

RESEARCH PAPER

The Enigmatic Type Icn Supernova 2024abvb Located \sim 22 kpc from Its Host Galaxy

J. Shi,¹ K. Auchettl,^{1,2} W. B. Hoogendam,^{3,4} D. Farias,⁵ N. Sarin,⁶ K. W. Davis,² N. Morrell,⁷ J. T. Hinkle,^{8,9,3,10} D. O. Jones,¹¹ C. Lidman,^{12,13} C. Angus,¹⁴ C. Ashall,³ C. R. Burns,¹⁵ D. D. Desai,³ A. Do,^{16,6} L. Galbany,^{17,18} E. Y. Hsiao,¹⁹ M. E. Huber,³ M. Y. Kong,³ B. Martin,¹² K. Medler,^{20,21} C. Pfeffer,³ A. Polin,²² L. Rauf,^{12,13} S. Romagnoli,¹ B. Schmidt,¹² B. J. Shappee,³ M. D. Stritzinger,²³ A. Syncatto,¹¹ B. E. Tucker,^{12,24} and M. A. Tucker^{25,26}

¹OzGrav, School of Physics, The University of Melbourne, Parkville, VIC, Australia

²Department of Astronomy and Astrophysics, University of California, Santa Cruz, CA, USA

³Institute for Astronomy, University of Hawai'i at Manoa, 2680 Woodlawn Dr., Hawai'i, HI 96822, USA

⁴NSF Graduate Research Fellow

⁵DARK, Niels Bohr Institute, University of Copenhagen, Jagtvej 128, 2200 Copenhagen, Denmark

⁶Kavli Institute of Cosmology Cambridge, Madingley Road, Cambridge CB3 0HA, United Kingdom

⁷Carnegie Observatories, Las Campanas Observatory, Casilla 601, La Serena, Chile

⁸Department of Astronomy, University of Illinois Urbana-Champaign, 1002 West Green Street, Urbana, IL 61801, USA

⁹NSF-Simons AI Institute for the Sky (SkAI), 172 E. Chestnut St., Chicago, IL 60611, USA

¹⁰NHFP Einstein Fellow

¹¹Institute for Astronomy, University of Hawai'i, 640 N. A'ohoku Pl., Hilo, HI 96720, USA

¹²The Research School of Astronomy and Astrophysics, Mt Stromlo Observatory, The Australian National University, Canberra, ACT 2611, Australia

¹³OzGrav, Centre for Gravitational Astrophysics, College of Science, The Australian National University, ACT 2601, Australia

¹⁴Astrophysics Research Centre, School of Mathematics and Physics, Queen's University Belfast, Belfast BT7 1NN, UK

¹⁵The Observatories of the Carnegie Institution for Science, 813 Santa Barbara St., Pasadena, CA 91101, USA

¹⁶Institute of Astronomy, Madingley Road, Cambridge CB3 0HA, United Kingdom

¹⁷Institute of Space Sciences (ICE-CSIC), Campus UAB, Carrer de Can Magrans, s/n, E-08193 Barcelona, Spain

¹⁸Institut d'Estudis Espacials de Catalunya (IEEC), 08860 Castelldefels (Barcelona), Spain

¹⁹Department of Physics, Florida State University, 77 Chieftan Way, Tallahassee, FL 32306, USA

²⁰Centre for Astrophysics and Supercomputing, Swinburne University of Technology, John St, Hawthorn, VIC 3122, Australia

²¹ARC Centre of Excellence for Gravitational Wave Discovery (OzGrav), John St, Hawthorn, VIC 3122, Australia

²²Department of Physics and Astronomy, Purdue University, West Lafayette, IN 47907, USA

²³Department of Physics and Astronomy, Aarhus University, Ny Munkegade 120, DK-8000 Aarhus C, Denmark

²⁴Australian National Centre for the Public Awareness of Science, The Australian National University, ACT 2601, Australia

²⁵Center for Cosmology and Astroparticle Physics, The Ohio State University, Columbus, OH, USA

²⁶Department of Astronomy, The Ohio State University, Columbus, OH, USA

Author for correspondence: J. Shi, Email: jennifer.shi@student.unimelb.edu.au.

(Received dd Mmm YYYY; revised dd Mmm YYYY; accepted dd Mmm YYYY; first published online 22 September 202X)

Abstract

We report multiwavelength observations of the highly offset (\sim 22.4 kpc) SN 2024abvb, the sixth Type Icn supernova to date. With a peak magnitude of $M_r = -19.55 \pm 0.11$ mag, it is among the most luminous in the existing sample and shows similar colours and decline rates to other SNe Icn. The early optical spectra show a blue continuum with narrow C II features ($\nu_{FWHM} \sim 2000 \text{ km s}^{-1}$), consistent with a typical wind velocity of a Wolf-Rayet star. The absence of C III $\lambda 5696$ emission at the time of explosion is consistent with a Type Ibn supernova; however, the lack of narrow He lines both in the optical and near-infrared spectra points towards a SNe Icn classification. Unlike the majority of SNe Icn, we do not detect broad features in the late-time (7 – 21 days relative to o -band peak) spectral phase of SN 2024abvb. Semi-analytical modelling of the light curves shows that it can be reproduced by $\sim 2.6 M_{\odot}$ of SN ejecta interacting with $\sim 0.3 M_{\odot}$ of circumstellar material (CSM); both larger than other SNe Icn but consistent with rapidly evolving SNe Ibn. The metallicity at the SN location is significantly lower than the global metallicity of its host galaxy, suggesting that line-driven mass loss, required to strip the progenitor of its H and He envelopes, was likely inefficient. We estimated the star formation rate history at the location of SN 2024abvb and find that it lies at the bottom \sim 5th percentile among SESNe hosts, which is inconsistent with a Wolf-Rayet progenitor. Based on its spectral features, local and host environment properties, and host-galaxy offset, we favour an $8 - 10 M_{\odot}$ star that is stripped by a compact companion as the progenitor that had a sufficient runaway velocity to reach the offset of SN 2024abvb.

Keywords: XXXXXXXXXXXXXXXX

1. Introduction

Stripped-envelope supernovae (SESNe) result from the core-collapse of massive stars $\gtrsim 8 M_{\odot}$, that have lost all or most

of their outermost H (or He) layers (e.g., Filippenko, 1997; Pastorello et al., 2007; Gal-Yam, 2017; Modjaz et al., 2019). Although the nature and evolution of SESNe progenitors re-

main uncertain^a, several mechanisms have been proposed to explain this envelope stripping. For example, radiative mass loss by line-driven winds (e.g., Heger et al., 2003; Smith, 2014), strong stellar winds from a single, H-deficient massive star (i.e., a Wolf-Rayet (WR) star with $M \gtrsim 25M_{\odot}$; e.g., Yoon, 2017), impulsive or eruptive mass loss (e.g., Dessart et al., 2010; Moriya, 2014; Smith, 2014) or from mass transfer to a binary companion (e.g., Podsiadlowski et al., 1992; Eldridge et al., 2013; Yoon et al., 2010; Götberg et al., 2017; Ercolino et al., 2025). In any of these scenarios, if the SN ejecta interacts with a dense circumstellar medium (CSM)^b, then the SN spectra during the photospheric phase will contain narrow emission lines – H for SN IIn (e.g., Schlegel, 1990), He for SN Ibn (e.g., Foley et al., 2007; Pastorello et al., 2008), C/O for SN Icn (e.g., Gal-Yam et al., 2022; Perley et al., 2022), and Si/S for SN Ien (e.g., Schulze et al., 2024). Such SNe provide a unique opportunity to probe the diverse mass loss histories and CSM distributions associated with massive stars (e.g., Fraser, 2020; Ercolino et al., 2025).

Type Ibn SNe (SNe Ibn) are a unique class of SESNe characterised by weak or absent H lines and narrow ($\nu_{\text{FWHM}} \sim 2000 \text{ km s}^{-1}$) He lines in their near-infrared (NIR) and optical spectra (e.g., Foley et al., 2007; Pastorello et al., 2007; Shaviv et al., 2017; Gal-Yam, 2017). The narrow He lines are interpreted as evidence of shock interaction between the rapidly moving SN ejecta and He-rich, but H-depleted, CSM surrounding the progenitor (Smith, 2017). SNe Ibn are rare, comprising only $\sim 1\text{-}2\%$ of core-collapse SNe (e.g., Pastorello et al., 2008; Ma et al., 2025; Pessi et al., 2025). Since the discovery of SN 2006jc, the prototypical SN Ibn, ~ 80 SNe Ibn have been spectroscopically classified on the Transient Name Server (TNS)^c.

Recently, population studies of SNe Ibn have begun to probe their formation channels and attempt to explain the origin of their dense CSMs (e.g., Hosseinzadeh et al., 2017; Maeda & Moriya, 2022; Ko et al., 2025a; Farias et al., 2025). Early studies of Type Ibn SN 2006jc suggested that massive WR stars ($\gtrsim 25M_{\odot}$) are possible progenitors of this class (Foley et al., 2007; Pastorello et al., 2007; Tominaga et al., 2008). However, studies of the environments of SNe Ibn (e.g., Hosseinzadeh et al., 2019; Dong et al., 2025; Warwick et al., 2025) and late-time observations of SN 2006jc identified a surviving companion (Maund et al., 2016; Sun et al., 2020), suggesting that (some) SNe Ibn explode in binary systems. This is also further supported by theoretical studies that have attempted to explain the low-metallicity environments, and the spectral and CSM properties of SNe Ibn using low mass He-stars found in binary systems (e.g., Maund et al., 2016; Dessart et al., 2022;

^aNote the recent discovery of hot ($T_{\text{eff}} \sim 50 - 100 \text{ kK}$), intermediate mass ($\sim 2 - 8 M_{\odot}$) helium stars whose hydrogen envelope has been stripped in a binary (Drout et al., 2023; Götberg et al., 2017). Their properties are consistent with stars that were stripped by binary interaction and have an initial mass between $\sim 8 - 25 M_{\odot}$, making them potential progenitors of SESNe.

^bThere is growing evidence that nearly 10% of all core-collapse SNe interact with dense CSM (e.g., Perley et al., 2020).

^cAs of 2026 Feb 17

Wu & Fuller, 2022; Ko et al., 2025b)

Type Icn SNe (SNe Icn) constitute a recently identified subclass of SESNe, even rarer than SNe Ibn. Based on their discovery and analysis of SN 2019hgp, Gal-Yam et al. (2022) defined SNe Icn as a distinct class, which had previously been theorised (Smith, 2017; Woosley, 2017). Only four additional SNe Icn have been reported since SN 2019hgp (SNe 2019jc, 2021csp, 2021ckj, 2022ann; Fraser et al., 2021; Perley et al., 2022; Pellegrino et al., 2022b; Davis et al., 2023). These SNe show narrow C, Ne, and O lines indicative of CSM interaction, while lacking H and He lines in their early spectra (Gal-Yam et al., 2022). More recently, Schulze et al. (2024) proposed a new SNe classification: Type Ien, following the discovery of SN 2021yfj (Gal-Yam et al., 2024a,b) whose spectra exhibit narrow Si, S, and Ar emission lines. Gal-Yam et al. (2024a) also proposed a potential intermediate class, Type Idn, whose spectra would primarily show O, Ne, and Mg lines. However, no SN with Type Idn spectral features have so far been discovered.

SNe Ibn and Icn are characterised by fast light curve evolution, rising to their peak brightness in $\lesssim 10$ days (Hosseinzadeh et al., 2017; Gal-Yam et al., 2022, although some events have longer rise times, for example, the Type Ibn SN 2010al Pastorello et al., 2015a). Their light curves typically reach peak luminosities of $r \approx -18.5$ mag. The rapid evolution suggests that the light curves are mainly powered by the SN shock interacting with a steep CSM profile (e.g., Maeda & Moriya, 2022; Nagao et al., 2023). The photometric properties, including spectroscopic evidence for shock interaction between the ejecta and H-poor CSM, resemble the properties seen in the emerging class of extremely rare SN-like stellar explosions known as “Luminous Fast Blue Optical Transients” (LFBOTs), which are thought to possibly result from the binary merger of a WR star with a companion (Metzger, 2022). However, if these SNe result from this evolutionary pathway, then it is thought that the delay time between the common-envelope phase and the merger is substantially longer than that inferred for LFBOTs (see Fig. 4 Metzger, 2022). Given the similarities between SNe Ibn and SNe Icn, it has been suggested that these events may represent a continuum of objects (e.g., Pellegrino et al., 2022b), with their features gradually varying along a spectrum of progenitor composition and mass-loss history. As such, discovering and analysing SNe Icn (in addition to SNe Ibn) can uncover new insights into the final evolution of massive stars found in binary systems and their explosion properties, allowing us to place them in the context of the SESNe population.

The origin of SNe Icn remains uncertain. However, due to the similarity in features between SN Ibn and SNe Icn, it is plausible that these events arise from related progenitor systems, such as the core-collapse of a WR star. However, understanding the exact progenitor system is complicated by the wide range of spectral properties observed in these objects. Based on the properties of SN 2019hgp, Gal-Yam et al., 2022 suggested that a spectroscopic subtype of WR stars that are C-rich and He-poor (WC stars) that underwent extreme mass loss before explosion are the progenitors of SNe Icn (with SNe Ibn arising

from WR stars that are He and N rich – WN stars). From the inferred ejecta parameters, environments, and explosion properties, Pellegrino et al. (2022b) suggested that there are multiple progenitor channels required to explain the diversity of properties associated with SNe Icn. More specifically, they suggest that the progenitor of SN 2019jc is an ultra-stripped star (a massive star in a close binary system that has most or all of its He being stripped), while SNe 2019hgp, 2021ckj, and 2021csp were consistent with WR stars. These progenitor systems likely experienced an extreme mass-loss episode (e.g., Perley et al., 2022 estimated a mass-loss rate of $0.5M_{\odot} \text{ yr}^{-1}$ for SN 2021csp), stripping away their He and possibly C layers. Other studies have also suggested that WR stars undergoing extreme mass loss are not the only progenitor channel for these SNe. Nagao et al. (2023) suggested that SNe 2021ckj and 2021csp both potentially originate from a merger of a WR star with a compact object. This merger produces an explosion ejecta that includes an aspherical, high-energy component and a spherical ejecta component. Assuming this progenitor channel, the authors argue that despite their photometric similarities, the differences in their spectral features are attributed to the viewing angles of the jets based on the amount of CSM observed along the line of sight: SN 2021ckj was observed from the polar direction, whereas SN 2021csp was observed from an off-axis direction. Based on the low-metallicity environment, low ejecta masses and low CSM velocities, Davis et al. (2023) favour a binary-stripping progenitor scenario over a single WR progenitor for SN 2022ann.

In the past two years, SNe with both Ibn and Icn spectral and photometric features have been discovered. For example, SN 2023emq (Pursiainen et al., 2023) was initially classified as a SN Icn due to the detection of a C III $\lambda 5696$ emission feature, also seen in SNe Icn SNe 2019hgp and 2021csp. At eight days after peak brightness, its spectra developed strong, narrow He I emission typical of SNe Ibn. However, some photometric properties were inconsistent with either class, leading Pursiainen et al. (2023) to tentatively conclude that SN 2023emq was a flash-ionised Type Ibn. Similarly, SN 2023xgo (Gangopadhyay et al., 2025b; Yamanaka & Nagayama, 2025) showed an early narrow C III $\lambda 5696$ feature reminiscent of SNe Icn, followed by He I emission after maximum light, resembling a SN Ibn. Gangopadhyay et al. (2025a) note that, if SN 2023xgo is interpreted as a flash-ionized SN Ibn, its unusually strong carbon emission would render it unique within this class. More recently, aside from SN 2023emq and SN 2023xgo, Farias et al. (2025) identified eight additional Ibn-like SNe that also exhibit a clear C III $\lambda 5696$ feature (see Figure A.3 in Farias et al. 2025). Due to their properties, these events offer novel insights into the extreme mass-loss histories and CSM distributions of massive star progenitors shortly before their death.

In this paper, we present an analysis of SN 2024abvb, one of the most luminous events among SNe Ibn and Icn classes. Optical spectra obtained 7.9 days before peak show SNe Ibn-like features (narrow He I and absent C III lines) while SNe Icn features (C II and O I P Cygni profiles) emerge 7.2 days after peak. These observations indicate that SN 2024abvb exhibits characteristics of both SN Icn and SN Ibn. Previous

observations of SN 2024abvb by Hu et al. (2026) suggest that its progenitor experienced extensive stripping of its outer layers prior to explosion. In addition, The INTEL Collaboration et al. (2026) report that SN 2024abvb exhibits a complex, nested structure in its CSM and is surrounded by a complex, nested CSM, indicating that the progenitor underwent multiple mass-loss episodes before core collapse. Here, we present a detailed multiwavelength analysis of SN 2024abvb and its host galaxy in the context of both the Type Icn and Ibn populations. This paper is structured as follows. In Section 2 we present the photometric and spectroscopic observations and data reduction procedures. In Section 3, we present our analysis of the host-galaxy environment, photometry, optical and NIR spectra, and compare these with SNe Ibn/Icn samples in the literature. We discuss our results and progenitor channels in Section 4 and conclude in Section 5.

Throughout the paper, we adopt a redshift $z = 0.0391 \pm 0.0002$, as determined in §3.3. This yields a distance modulus of $\mu = 36.2 \pm 0.01$ mag (where the uncertainty is determined from the redshift uncertainty) or luminosity distance of 172 ± 1 Mpc (assuming a flat Λ CDM cosmology with $H_0 = 70 \text{ km s}^{-1} \text{ Mpc}^{-1}$ and $\Omega_m = 0.3$). We adopt a foreground Milky Way extinction of $E(B - V)_{MW} = 0.16$ mag (Schlafly & Finkbeiner, 2011) toward SN 2024abvb, and all analyses are performed using Milky Way corrected light curves. We assume a negligible host extinction for SN 2024abvb owing to its large projected offset of ~ 22.4 kpc (see Section 3.1 for more detail) from its host galaxy and due to the lack of a Na I D absorption line seen in our spectra (see Figure A1).

2. Observations

SN 2024abvb was discovered by the Asteroid Terrestrial-impact Last Alert System Project (ATLAS; Tonry et al., 2018; Smith et al., 2020) in the cyan (c) band with an apparent magnitude of (18.78 ± 0.05) mag on November 22, 2024 (MJD 60636.33) as ATLAS24qlh (see Figure 1). The last ATLAS non-detection ($c > 19.4$ mag) occurred one day earlier, on November 21, 2024 (Tonry et al., 2024). The SN is associated with the host galaxy, PSO J011055.760-054416.73, with an offset of 22.4 kpc from the core of the host (see Figure 1; and Section 3.1 for more discussion about the host properties). SN 2024abvb was classified on November 27, 2024, at UT 12:33:29 (6 days after discovery) as a SN Icn (Stritzinger et al., 2024) based on a spectrum taken with the 2.56-m Nordic Optical Telescope (NOT) equipped with the Alhambra Faint Object Spectrograph and Camera (ALFOSC) as part of the NOT Unbiased Transient Survey.

2.0.1 Survey Photometry

Photometry of SN 2024abvb was obtained from public ATLAS (Tonry et al., 2018; Smith et al., 2020) and Zwicky Transient Facility (ZTF; Bellm et al., 2019) surveys. ATLAS data were retrieved from the ATLAS Transient Science Server (Smith et al.,

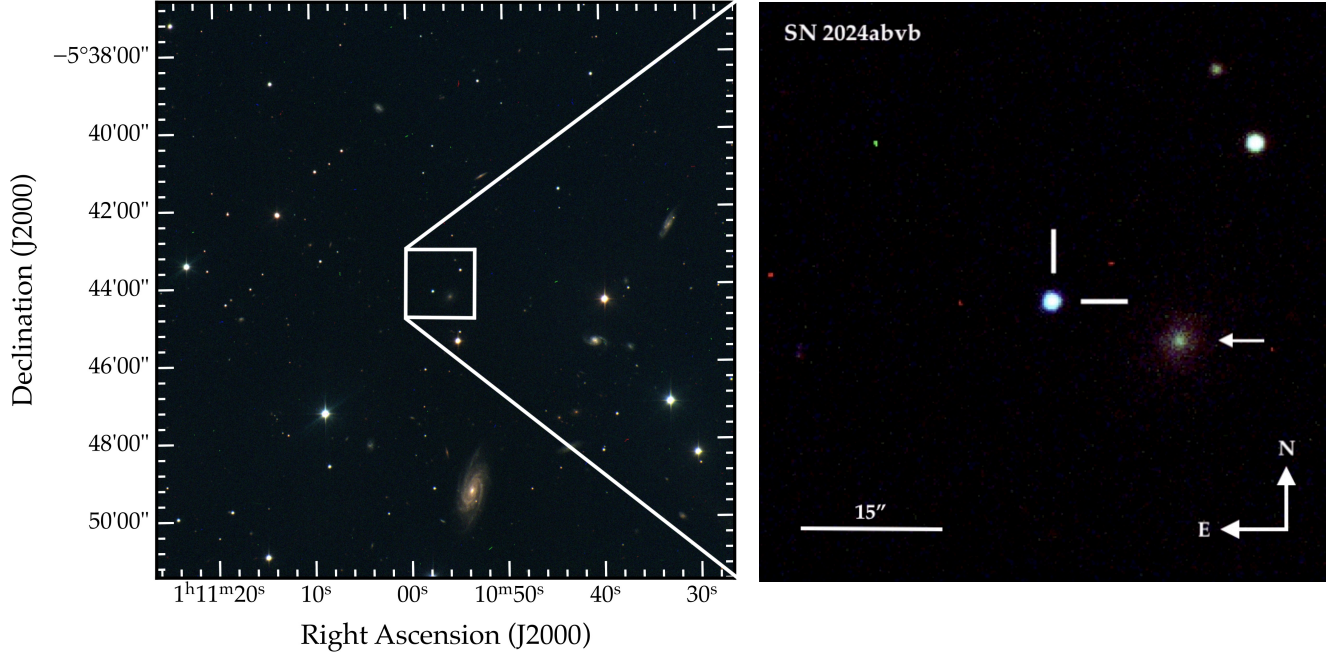


Figure 1. The left panel is a $15' \times 15'$ image of SN 2024abvb constructed using multi Bgr -band Swope images that are mapped to the blue, green, and red channels of the image, respectively. The right panel is a $2' \times 2'$ cutout with the position of SN 2024abvb marked. The arrow indicates the host galaxy PSO J011055.760-054416.73 with an apparent magnitude of $m_{AB} = 18.27$ mag (Flewelling et al., 2020).

2020) with photometry derived using ATClean^d (Rest et al., 2025), which is based on procedures presented in (Davis et al., 2023). Likewise, ZTF observations were obtained through the ZTF forced photometry service (Masci et al., 2019, 2023) and standard baseline corrections to the data and a signal-to-noise threshold of 3 were used, following the procedure outlined in the ZTF forced photometry manual v2.3^e. We also collected riw -band photometry of SN 2024abvb before and during the event from the Panoramic Survey Telescope and Rapid Response System (Pan-STARRS; Kaiser et al., 2010; Chambers et al., 2016) Survey for transients (PSST; Huber et al., 2015). Observations were performed using standard PSST procedures as outlined in Huber et al. (2015).

2.0.2 Follow-up Photometry

Complementing the initial survey detections, we acquired targeted follow-up photometry to obtain additional multi-band measurements of SN 2024abvb. The University of Hawai'i-owned and operated UKIRT 3.8m telescope observed SN 2024abvb with the NIR-imaging Wide Field Camera (WFCAM; Casali et al. 2007; Hodgkin et al. 2009). The data reductions follow those presented in Hoogendam et al. (2025a,b). Briefly, the data were processed using photpipe (Rest et al., 2005) and calibrated relative to 2MASS photometry of nearby field stars, following the methods described by Hodgkin et al. (2009) and Peterson et al. (2023). We do not perform image subtraction when we run DOPHOT (Schechter et al., 1993) as part of photpipe. There is negligible host-galaxy flux at the loca-

tion of SN 2024abvb because of its large offset. Therefore, we consider local background estimation and centroid determination from individual images sufficient to obtain reliable photometry.

Ultraviolet and optical photometry were obtained with the *Neil Gehrels Swift Observatory* (*Swift*; Gehrels et al., 2004) UV-Optical Telescope (UVOT; Roming et al., 2005) using the Poole et al. (2008) zero points updated by Breeveld et al. (2010) and Breeveld et al. (2011). We used HEASoft^f version 6.33.2 to obtain aperture photometry with the UVOTSOURCE package. An aperture of $5''$ is used for the source and a $20''$ source-free region located at $(\alpha_{J2000}, \delta_{J2000}) = (1^h 10^m 58^s 77, -05^\circ 43' 26'' 58)$ is used for the background.

Additional optical photometric observations were taken as part of the Precision Observations of Infant Supernovae Explosions (POISE; Burns et al., 2021) Collaboration using the 1m Swope telescope located at the Las Campanas Observatory (LCO). Photometric reductions follow the procedures described in Krisciunas et al. (2017).

The complete multi-band light curve of SN 2024abvb is shown in Figure 2. While ATLAS was the first to discover SN 2024abvb, Pan-STARRS (Chambers et al., 2016) detected the source with an observed apparent magnitude of (19.9 ± 0.05) mag (corresponding to an absolute magnitude of (-16.2 ± 0.05) mag) on MJD 60635.3 (≈ 1 day prior to ATLAS's discovery) in the w -P1 filter. BlackGEM (Groot et al., 2024) measured the SN about five days after (MJD 60640) in the BG- q -BlackGem filter at an apparent magnitude of (17.5 ± 0.02) mag (corresponding to an absolute magnitude

^d<https://github.com/srest2021/atclean>

^ehttps://irsa.ipac.caltech.edu/data/ZTF/docs/ztf_forced_photometry.pdf

^f<https://heasarc.gsfc.nasa.gov/docs/software/heasoft>

of (-18.9 ± 0.02) mag). The last non-detections (denoted by empty coloured triangles in Figure 2) prior to discovery are from ATLAS ($o > 19.2$ mag, 5σ ; $c > 19.4$ mag, 5σ) and ZTF ($g > 20.5$ mag, 5σ) which were obtained 10.9, 10.1, and 11.0 (MJD 60634.4, 60635.1, and 60634.3) days before o -band maximum brightness, respectively.

2.0.3 X-ray

In addition to the *Swift* UVOT observations, contemporaneous X-ray observations were obtained using *Swift*'s X-ray Telescope (XRT; Burrows et al., 2005) in photon-counting mode. All observations were reprocessed from level one XRT data using XRTPIPELINE version 0.13.7 with the most up-to-date calibrations, standard filters, and screening. Using a source region of radius $30''.0$ centred on the position of SN 2024abvb and a source-free background region of radius $150''.0$ located at $(\alpha_{J2000}, \delta_{J2000}) = (1^h 11^m 10.6583^s, -5^\circ 39' 31.574'')$, we find no significant X-ray emission associated with the SN in the individual epochs. To increase the signal-to-noise of observations, we merged all individual *Swift* XRT observations using XSELECT version 2.5b and derived a 3σ upper limit of 0.001 counts/second in the 0.3–10.0 keV energy range. Following Farias et al. (2025), we assume an absorbed thermal Bremsstrahlung model with a temperature of 2.3 keV and a Galactic column density of $6.70 \times 10^{20} \text{ cm}^{-2}$ to convert this aperture-corrected count rate into a 3σ upper limit on the flux (and luminosity). We obtain a 3σ upper limit to the unabsorbed flux of $3.49 \times 10^{-14} \text{ erg cm}^{-2} \text{ s}^{-1}$, which corresponds to a 3σ upper limit to the unabsorbed X-ray luminosity of $1.26 \times 10^{41} \text{ erg s}^{-1}$.

2.1 Spectroscopy

Our optical spectra consist of two spectra from NOT, four spectra from the SuperNova Integral Field Spectrograph (SNIFS; Lantz et al., 2004) on the University of Hawai'i 2.2-meter (UH 2.2m) telescope as part of the Spectroscopic Classification of Astronomical Transients programme (SCAT; Tucker et al., 2022), four spectra using the The Wide Field Spectrograph (WiFeS) that is mounted on the Australian National University 2.3 metre (ANU 2.3m) telescope (Dopita et al., 2007, 2010; Price et al., 2024), one spectrum from the Inamori Magellan Areal Camera and Spectrograph (IMACS) on the 6.5 m Magellan-Baade telescope (Dressler et al., 2011), and a final spectrum from the Keck-II 10.0 m telescope using the Keck Cosmic Web Imager (Morrissey et al., 2018).

SNIFS reductions used the pipeline presented in Tucker et al. (2022). The WiFeS spectra were taken in “Nod & Shuffle” mode, which produced simultaneous science and sky spectra, of which the sky contribution is subtracted during reduction (see Section 2.2 of Carr et al., 2024, for more details). The observations were reduced using the default reduction pipeline pyWiFeS (Childress et al., 2014) to produce calibrated 3D data cubes, of which 2D spectrum were extracted. NOT data were reduced following standard techniques using pyraf scripts within the ALFOSC GUI environment developed by E.

Cappellaro. The flux calibration for the NOT spectra was performed using nightly sensitivity functions derived from standard star observations. An IMACS spectrum was obtained on Dec. 10, 2024 by A. Polin. Reductions were carried out through standard IRAF^g routines. Flux and telluric corrections were performed with appropriate standards observed during the same night. KCWI reductions were performed using the Keck Cosmic Web Imager Data Reduction Pipeline (KCWI DRP)^h. The flux calibration was based on spectrophotometric standard stars observed on the same night as SN 2024abvb.

Our NIR spectrum was taken on the 3.0m NASA Infrared Telescope Facility (IRTF) with SpeX (Rayner et al., 2003) in PRISM mode as part of the Hawai'i Infrared Supernova Study (HISS; Medler et al., 2025). Reductions were performed with the Sextool (Cushing et al., 2004), including telluric correction using an A0V star, as in Hoogendam et al. (2025a,b).

A low-resolution spectrum covering the wavelength range 0.8–2.5 μm was obtained on 2024 December 8.04 UTC (MJD 60652.04) at an airmass of 1.1, with the Folded Port Infrared Echellette (FIRE) spectrograph on the 6.5 m Magellan Baade Telescope (Simcoe et al., 2008). The observation consisted of standard ABBA loops on the science target, totalling 507 s of on-target exposure time, followed immediately by an observation of the telluric standard HD4329. Detailed observational setup and reduction procedures are described by Hsiao et al. (2019). A table of our spectroscopic observations is presented in Table A1.

3. Analysis

3.1 Host Galaxy Environment

We estimate the galactic properties of PSO J011055.760–054416.73, the host galaxy of SN 2024abvb, using the `Blast` tool (Jones et al., 2024)ⁱ. `Blast` uses host-galaxy photometry and PSF-matched elliptical apertures from Galaxy Evolution Explorer (Martin et al., 2005), Sloan Digital Sky Survey (Fukugita et al., 1996; York et al., 2000), 2MASS (Skrutskie et al., 2006), Wide-field Infrared Survey Explorer (Wright et al., 2010), Dark Energy Survey (Dey et al., 2019), and Pan-STARRS (Chambers et al., 2016). The global spectral energy distribution (SED) properties are measured using `Prospector` (Leja et al., 2019; Johnson et al., 2021; Wang et al., 2023).

The global properties of the host galaxy of SN 2024abvb are displayed in Table 1. The reported values and uncertainties are the median and 16th and 84th percentiles of the posterior distributions. The derived stellar mass ($\sim 10^{9.7} M_\odot$) is below the mass of typical large galaxies ($10^{10} M_\odot < M < 10^{11} M_\odot$) and above dwarf galaxies ($M < 10^8 M_\odot$), which suggests it is an intermediate-mass galaxy. The host galaxy also has moder-

^gThe Image Reduction and Analysis Facility (IRAF) is distributed by the National Optical Astronomy Observatory, which is operated by the Association of Universities for Research in Astronomy, Inc., under cooperative agreement with the National Science Foundation.

^hAccessible via <https://kcwi-drp.readthedocs.io/en/latest/index.html>.

ⁱ<https://blast.scimma.org/>.

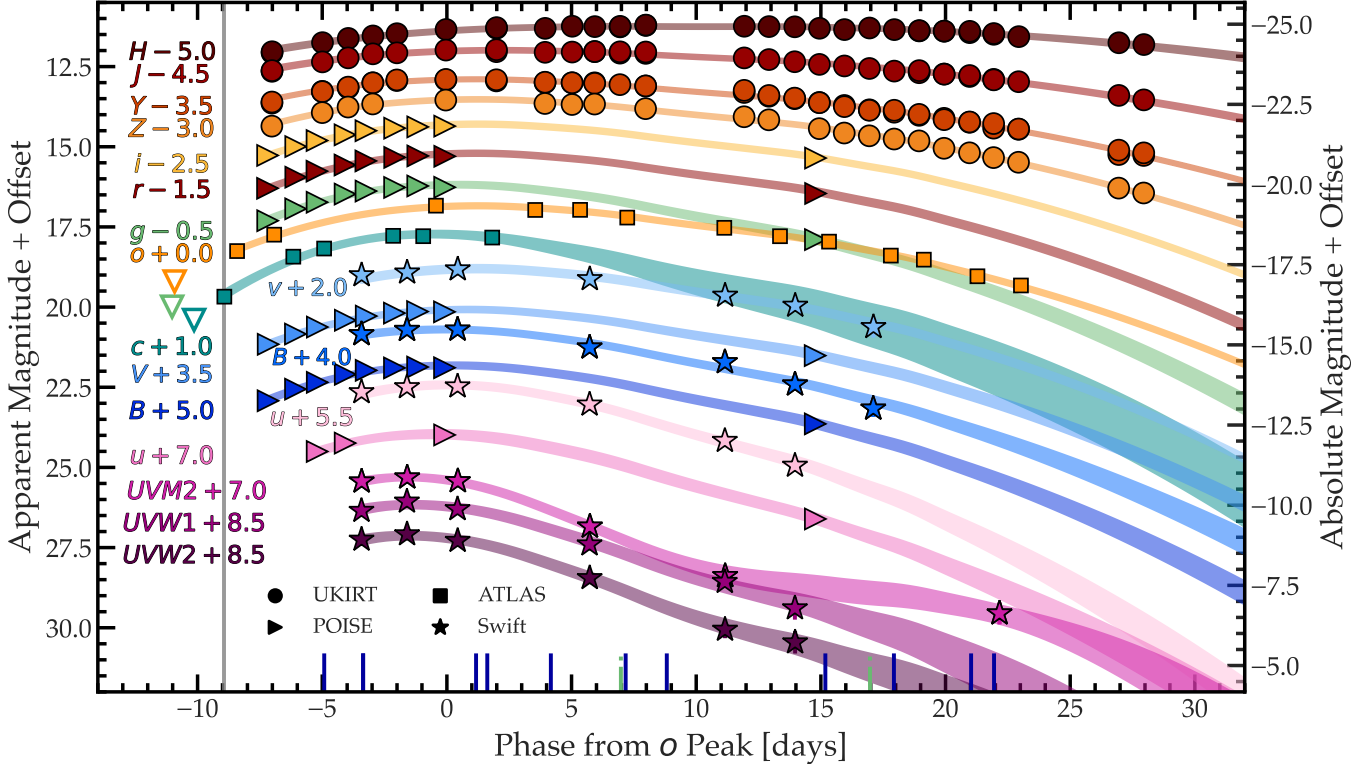


Figure 2. The UV, optical, and NIR light curves of SN 2024abvb. Upper limits are denoted with hollow triangles. The grey solid line indicates the time of discovery (MJD 60636.3), which is 3 days after the estimated time of explosion (MJD 60633.4). The spectral epochs with optical (NIR) spectra are highlighted with solid blue (dashed green) lines. The phase is given relative to the o -band maximum (MJD 60645.3). To guide the eye, shaded interpolation curves are overlaid for each filter band, indicating the Gaussian process fits within 1σ .

ate star-formation ($\sim 0.1 M_{\odot} \text{yr}^{-1}$) and sub-solar metallicity ($\sim 0.04 Z_{\odot}$), approximately an order of magnitude lower to that of the Large Magellanic Cloud. We caution, however, that this metallicity estimate is derived solely from photometric measurements and may therefore be subject to significant uncertainty.

Table 1. Global properties of the host galaxy of SN 2024abvb.

Parameter	Value	Units
Stellar Mass M_{\ast}	$9.66^{+0.12}_{-0.12}$	$\log_{10}(M_{\odot})$
Star-Formation Rate (SFR)	$-0.99^{+0.80}_{-1.22}$	$\log_{10}(M_{\odot} \text{ yr}^{-1})$
Specific Star-Formation Rate (sSFR)	$-10.62^{+0.79}_{-1.22}$	$\log_{10}(\text{yr}^{-1})$
Stellar Metallicity Z_{\ast} ^a	$-1.38^{+0.38}_{-0.34}$	$\log_{10}(Z_{\odot})$
Mean Stellar Age	$7.93^{+3.78}_{-1.04}$	Gyr

^aWe note that this metallicity estimate is derived from photometric measurements alone and may not be robustly constrained.

Figure 3 shows the SFR against stellar mass for the hosts of SNe Ibn (Farias et al. in prep.; Sanders et al. 2013; Dong et al. 2025; green squares), SNe Icn (Davis et al., 2023; Gal-Yam, 2017; Perley et al., 2022; Pellegrino et al., 2022b; orange circles), SNe IIn from PTF (Schulze et al., 2022; grey circles), and transitional SNe Ibn/Icn candidates (Pursiainen et al., 2023; Gangopadhyay et al., 2025b; purple and blue triangles). Host-

galaxy parameters for the SNe IIn sample taken from Schulze et al. (2022) were extracted using Prospector (implemented in Blast), and the SNe Ibn sample taken from Farias et al. (in prep.) also used Blast. Because most of the SNe Icn and transitional Ibn/Icn candidates were originally modelled with different spectral energy distribution (SED) fitting methods, we re-derived their host-galaxy properties using Blast to ensure consistency across the full sample. The left panel of Figure 3 shows that the host galaxy of SN 2024abvb has a slightly lower SFR than the majority of SNe Ibn and SNe IIn hosts, while lying between the two transitional candidates. Its stellar mass is consistent with the median of galaxies hosting SESNe and SNe IIn. In comparison to the SNe Icn sample, SN 2024abvb has an SFR and stellar mass most consistent, within uncertainties, with SN 2021csp (Perley et al., 2022). The right panel of Figure 3 shows the relationship between the Specific Star-Formation Rate (sSFR) and stellar mass for our SNe samples. Overall, we find that the sSFR declines with stellar mass, indicating that more massive galaxies are less efficient at forming stars per unit stellar mass. At its given stellar mass, the host galaxy of SN 2024abvb lies toward the middle to lower end of the sSFR distribution, which may suggest that a progenitor outlived the primary episode of star formation or, statistically less likely, exploded before other high-mass stars formed (Davis et al., 2023).

Figure 4 shows the projected distance between the su-

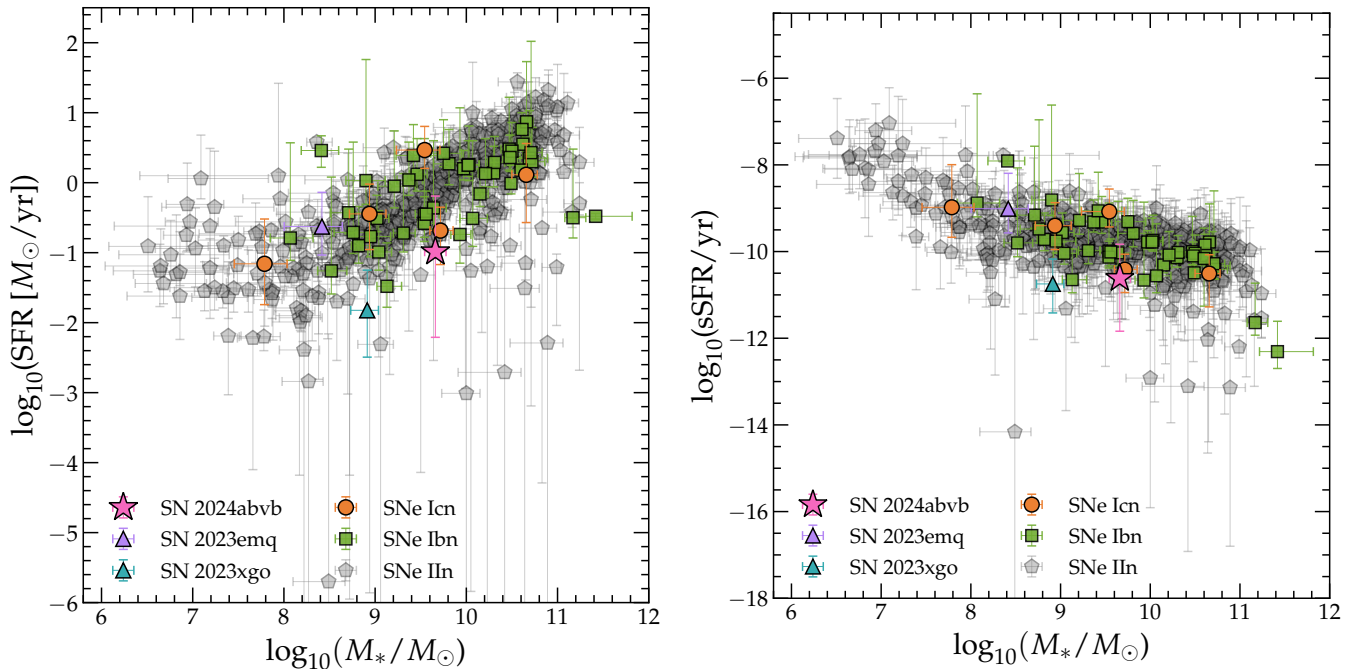


Figure 3. Left: The host-galaxy stellar mass versus star formation rate (SFR) for SESNe and SNe IIn. SN 2024abvb ($\log_{10}(M_*/M_\odot) = 9.66^{+0.12}_{-0.12}$) is denoted with the pink star. The SNe IIn sample (taken from Schulze et al. (2022)) is shown as grey pentagons, the SNe Ibn (taken from Farias et al. in prep.) are shown as green squares, and the SNe Icn are shown as orange circles. Using Blast (Jones et al., 2024), we also compare SN 2024abvb to SN 2023emq (purple triangle) and SN 2023xgo (blue triangle), the two transitional SNe Ibn/Icn candidates found in the literature. Right: We compare the host-galaxy stellar mass and the Specific Star-Formation Rate (sSFR) for SESNe and SNe IIn.

pernova and its host galaxy versus the stellar mass for our interacting SESNe sample. Interestingly, SN 2024abvb has the largest projected distance (22.4 kpc) compared to other SNe Icn. SN 2024acyl (Dong et al., 2025), a SN Ibn, has the (currently) largest known projected offset from its host galaxy, at ~ 35 kpc. A small number of other SNe Ibn also have similar projected distances as SN 2024abvb, but they are hosted by larger host galaxies. Among the SNe Ibn and SNe Icn, there is a tentative trend that a larger stellar mass corresponds to a greater offset from its SN and this is supported by SN 2024abvb and SN 2024acyl. In the SNe-Icn sample, SN 2019jc has the second largest offset (11.2 kpc), which is half the projected distance of SN 2024abvb. The two SNe Ibn with comparable offsets to SN 2024abvb are SN 2000er (Pastorello et al., 2008) and LSQ13ccw (Pastorello et al., 2015b), but both events are associated with larger host galaxies ($\log_{10}(M_*/M_\odot) = 11.17^{+0.14}_{-0.09}$ and $\log_{10}(M_*/M_\odot) = 10.71^{+0.12}_{-0.09}$, respectively).

At its projected distance, the host galaxy of SN 2024abvb exhibits a SFR lower than that of SNe Ibn hosts, as shown in the middle panel of Figure 4. In contrast, when compared with transitional candidates and SNe Icn, SN 2024abvb shows the largest projected distance at its given SFR, however this is likely reflective of the small sample size of identified transitional sources and SNe Icn.

We compare the host-galaxy metallicity to the projected offset in Figure 4 (right). Again, we caveat that the metallicity estimates for the sample rely solely on photometric data and should be interpreted with caution due to significant uncer-

tainties. The median metallicity values for all the interacting SESNe are slightly below solar metallicity, which suggests that a subsolar-metallicity host environment may be necessary to produce interacting SESNe, although we note that there are large uncertainties associated with our sample. SN 2024abvb has metallicity values consistent, within uncertainties, to 38% of the SNe Ibn population, and matches both the transitional SNe Ibn/Icn candidates (i.e., SN 2023xgo ($\log_{10}(Z_*/Z_\odot) = -1.09^{+0.30}_{-0.34}$) and SN 2023emq ($\log_{10}(Z_*/Z_\odot) = -1.20^{+0.88}_{-0.53}$)), and two of the five SNe Icn (i.e., SN 2019jc ($\log_{10}(Z_*/Z_\odot) = -1.03^{+0.24}_{-0.34}$), and SN 2021csp ($\log_{10}(Z_*/Z_\odot) = -1.09^{+0.37}_{-0.43}$)). If we instead use the galaxy mass–metallicity relation of Tremonti et al. (2004), we find that the host galaxy of SN 2024abvb is estimated to have a metallicity of $12 + \log(\text{O/H}) = 8.86$, corresponding to $\log_{10}(Z_*/Z_\odot) = 0.17$, assuming Asplund et al. (2009) abundances. Again, this is consistent within uncertainties with the host metallicities associated with our SESNe sample, but particularly the SESNe in our sample that are found in approximately solar-like metallicity environments. However, we note that given the large offset of SN 2024abvb from its host galaxy, the metallicity at the explosion site is likely lower than this global estimate.

Overall, we find that despite its large projected offset to its host, the host of SN 2024abvb is consistent with the host properties of the population of interacting SESNe.

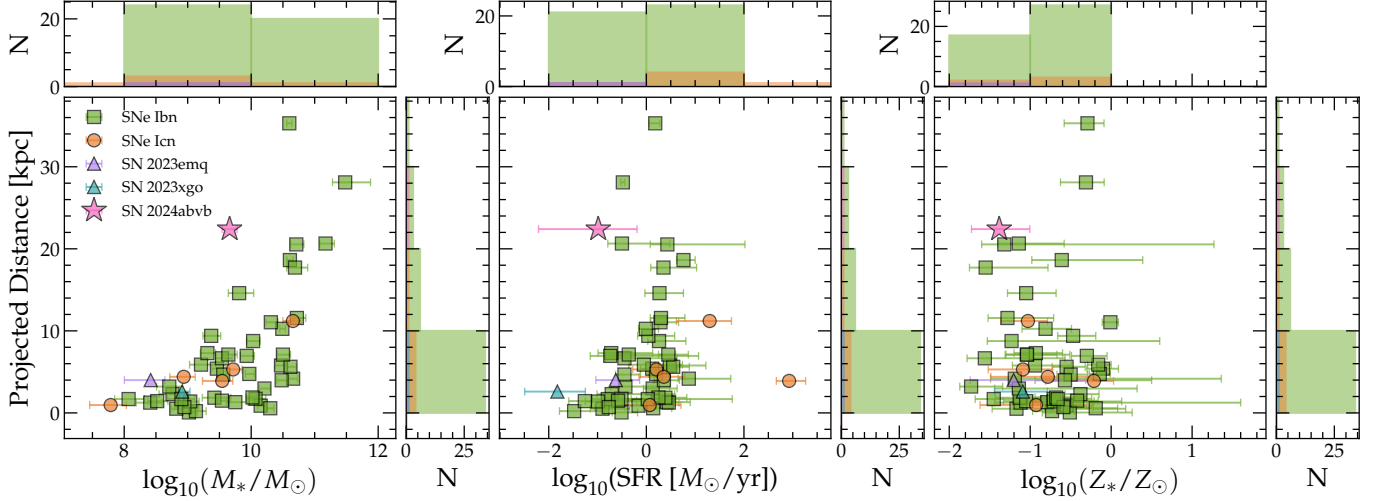


Figure 4. Histograms and scatter plots of the host galaxy properties of interacting SESNe against projected distance. SNe Ibn (green squares, 44) are collected from Farias et al. (in prep.), Sanders et al. (2013) and Dong et al. (2025), while the SNe Icn (orange circles, 5), transitional SNe Ibn/Icn candidates (purple and blue triangles), and SN 2024abvb (pink star) data are from B1ast (Jones et al., 2024). The markers are the same across all three plots. The vertical uncertainty for SN 2024abvb is smaller than the plotted star, as the projected distance is derived from a distance modulus with a 0.1 mag uncertainty. The top histograms across the three plots show the number (N) of SNe per stellar mass, SFR, or stellar metallicity, respectively. *Left:* host-galaxy stellar mass vs. projected distance. *Middle:* SFR vs. projected distance. *Right:* stellar metallicity vs. projected distance. SN 2024abvb has the largest projected offset amongst the SNe Icn and transitional SNe Ibn/Icn candidates, while its host-galaxy properties are broadly consistent with the SESNe population.

3.2 Photometric properties and evolution

SN 2024abvb has a similar rise and decline in all UV, Optical and NIR bands. We estimate the peak dates and magnitudes in the o - and g -bands using the Gaussian Process interpolation from the PYTHON package `george` (Foreman-Mackey, 2015) with a Matern 3/2 kernel. The o -band maximum is estimated to be 60645.3 ± 0.9 MJD, while the g band peaks at MJD 60644.0 ± 1.5 . We define the rise time as the time between the explosion and the peak date of the o band. Using the time of explosion as estimated in Section 3.2.1, the rise time of SN 2024abvb from explosion to maximum is $11.9^{+1.1}_{-1.2}$ days. This rise-time is comparable to that of SN 2022ann (~ 10 days; Davis et al. 2023), and consistent with two of the SNe Ibn rise-times reported in Hosseinzadeh et al. (2017), in particular PS1-12sk (13.3 ± 4.7 days), SN 2014ak (10.3 ± 3.9 days), and SN 2024acyl (11.3 ± 0.2 days) (Dong et al., 2025). The rapid rise to peak brightness can be attributed to the CSM interaction, which can produce a fast increase in luminosity as the SN shock propagates through and expels the surrounding CSM and ejecta upwards (Perley et al., 2022).

Following Section 4.2 of Panjkov et al. (2024), we search for evidence of pre-explosion variability from the progenitor of SN 2024abvb. We found no evidence for pre-explosion variability in the Pan-STARRS w , r , or i bands for the progenitor of SN 2024abvb. The deepest constraint is provided by the w band, which has the most extensive pre-explosion coverage, yielding a luminosity limit on the progenitor to be $\approx 1.0 \times 10^5 L_\odot$ (3σ).

Figure 5 compares the r - and g -band absolute magnitude light curves of SN 2024abvb with other interaction-powered SESNe. Compared to the SNe Icn sample, taken from (Davis

et al., 2023; Pellegrino et al., 2022b; Gal-Yam et al., 2022), SN 2024abvb is noticeably brighter in both bands (M_r peak $= -19.55 \pm 0.11$ mag, M_g peak $= -19.61 \pm 0.11$ mag), similar to SN 2021ckj and SN 2021csp. SNe Icn show a wide range in peak magnitudes spanning ~ 3 mag, from the faintest event SN 2019jc to SN 2021csp, which reaches magnitudes comparable to those of superluminous SNe (e.g., Angus et al., 2019). SN 2024abvb is brighter than the canonical SN Ibn, SN 2006jc, and has a similar shape in its rise to the SNe Ibn template, although Hosseinzadeh et al. (2017) highlights that the template is biased towards brighter, slow-rising transients. In comparison to the two transitional SNe Ibn/Icn sources (SN 2023xgo Gangopadhyay et al., 2025b and SN 2023emq Pursiainen et al., 2023) SN 2024abvb is roughly 1.2 (1.85) mag brighter in the g (r) band.

SN 2024abvb declines at 0.07 ± 0.007 mag day $^{-1}$ over two weeks in the r band, assuming a constant post-peak decline despite the observational gap between ~ 11 and $+26$ days after explosion. Compared to other SNe Icn, the decline rate (a week after peak brightness) of SN 2024abvb is similar to SN 2019hgp, SN 2019jc, and SN 2021ckj while roughly double the rate of SN 2022ann (10 days after its peak). This rate is also slightly lower than that of the SN Ibn sample (0.1 mag day $^{-1}$ within 30 days post-maximum) (Hosseinzadeh et al., 2017). In contrast, SN 2023emq declines at roughly twice the rate (~ 0.2 mag day $^{-1}$) over two weeks after peak, which Pursiainen et al. (2023) note is at the extreme end of SNe Ibn/Icn. Hosseinzadeh et al. (2017) argue that such rapid decline rates (0.05 – 0.15 mag day $^{-1}$) rule out radioactive decay as a significant power source for the late-time light curves (except for a significant outlier, OGLE12-06) and instead supports circumstellar interaction as the most likely power source, consistent with the literature.

SN 2024abvb exhibits a g -band evolution similar to that in the r band, with a steep rise and a short-lived peak. Its g -band decline rate is $0.1 \text{ mag day}^{-1} \pm 0.001$, similar to SN 2023xgo ($0.14 \text{ mag day}^{-1}$), but nearly three times faster than the relatively flat decline of SN 2022ann ($0.035 \text{ mag day}^{-1}$).

In Figure 6 we show the colour evolution of SN 2024abvb compared with the same SNe in Figure 5. Near the maximum phase, SNe Icn on average are bluer than the transitional sources. The colour evolution of SN 2024abvb remains consistently flat for the initial six days and grows redder over the subsequent fortnight. SN 2021csp and SN 2019hgp follow a similar evolution during their initial 30 days, while SN 2022ann begins significantly blue at maximum phase and grows redder. This broadly consistent colour evolution may indicate a long-lasting circumstellar interaction (CSI) powering source (Pellegrino et al., 2022b; Perley et al., 2022). In contrast, SN 2023xgo and SN 2023emq show markedly redder colours during the first ten days (albeit with only three data points), differing from the evolution seen in SN 2024abvb. Overall, the colour evolution of SN 2024abvb exhibits features seen in both SNe samples.

3.2.1 Time of first light

Under the assumption that the first light occurs at the same time in all bands, we estimate the time of explosion for SN 2024abvb by fitting the ATLAS forced photometry to a two-component power-law model (similar to other studies, e.g., Vallely et al., 2021; Fausnaugh et al., 2023; Hoogendam et al., 2024, 2025a,b) defined as

$$f(t) = \begin{cases} 0 & t < t_0 \\ A \left(\frac{t-t_0}{1+z} \right)^\alpha & t \geq t_0, \end{cases} \quad (1)$$

where

$$\alpha \equiv \alpha_1 \left(1 + \frac{\alpha_2(t-t_0)}{1+z} \right). \quad (2)$$

The inferred value of α in the one-component model depends on the fraction of the rising light curve included in the fit (e.g., Vallely et al., 2021), but the α_1 parameter from the two-component model remains insensitive. Rather, the parameters α_1 and α_2 correspond to the rise slope and the term necessary to trace the light curve peak curvature, which serves to minimise biases in α_1 (see Vallely et al., 2021, for more details). t_0 is the time of first light, A is a constant, and z is the redshift. We fit the data using the `emcee` package (Foreman-Mackey et al., 2013), with results presented in Figure 7 and Table 2. The fitted time of explosion is MJD $60633.4^{+0.3}_{-0.2}$, ~ 3 days before discovery (MJD_{discovery} = 60636.33), 4.0 (28.9) days before our first optical (NIR) spectrum, and 11.9 days before o -band maximum.

3.2.2 Bolometric Analysis

From our multiwavelength light-curve coverage, we estimate the bolometric properties using `extrabol` (Thornton et al., 2024). After a series of blackbody SEDs is fit to the broadband

Table 2. Best-fit parameters to the rising light curve of SN 2024abvb as shown in Figure 7.

Quantity	Value	Units	Description
t_0	$60633.38^{+0.26}_{-0.22}$	MJD	Time of first light
α_{o_1}	$2.15^{+0.14}_{-0.13}$		o -band rise slope
α_{o_2}	$-0.024^{+0.001}_{-0.001}$		o -band decline slope
A_o	$0.01^{+0.01}_{-0.01}$	mJy	o -band constant
α_c_1	$2.64^{+0.21}_{-0.19}$		c -band rise slope
α_c_2	$-0.02^{+0.01}_{-0.01}$		c -band decline slope
A_c	$0.01^{+0.01}_{-0.01}$	mJy	c -band constant

light curves, `extrabol` infers the luminosity, photospheric radius, and temperature evolution.

Figure 8 presents the bolometric light curve and the blackbody radius and temperature evolution of SN 2024abvb, based on 15 photometric light curve epochs spanning the UVOT UV to the UKIRT IR bands. The bolometric luminosity of SN 2024abvb follows an approximately linear decline from ~ 6 –30 days after explosion. SN 2024abvb rises to a peak of $\sim 11,000$ K within six days and rapidly cools over the next 25 days to approximately 4000 K. SN 2024abvb exhibits a blackbody radius evolution not seen in other SNe Icn or Ibn. Its radius rapidly shrinks when it reaches its maximum temperature and then gradually expands to 6.1×10^{15} cm at 32 days after the time of explosion. From there, the radius plateaus to a radius of $\sim (5 - 6.1) \times 10^{15}$ cm.

The top panel of Figure 8 shows a comparison of SN 2024abvb's bolometric luminosity with our SNe Ibn and SNe Icn samples. About three days before maximum, SN 2024abvb has a peak luminosity of 4×10^{43} erg s $^{-1}$, making it one of the brighter sources in our sample, similar to SN 2019hgp, SN 2022ann, and SN 2021csp ($\sim 3 \times 10^{43}$ erg s $^{-1}$, $\sim 4 \times 10^{43}$ erg s $^{-1}$, $\sim 3.5 \times 10^{43}$ erg s $^{-1}$, respectively). The bolometric luminosity evolution of SN 2024abvb is similar to that of SNe Ibn and transitional events. Its rise to peak brightness and decline until ~ 25 days after peak closely follows the SNe Ibn template (Hosseinzadeh et al. (2017); grey band). Although the transitional SNe Ibn/Icn candidates and selected SNe Ibn sources are less luminous, they exhibit comparable luminosity evolution. After ~ 25 days, SN 2024abvb fades quickly, resembling SN 2022ann (Type Icn; Davis et al., 2023).

The middle panel of Figure 8 compares the blackbody radius of SN 2024abvb with the interacting SNe sample. SN 2024abvb has the largest photospheric radius of all SNe Ibn/Icn in our sample. Its evolution is akin to SN 2022ann from 5 days before peak, in which the radii begins to recede much later (~ 20 days after peak brightness) compared to the other objects that recede within a week after the maximum. During the first three weeks after peak luminosity, the estimated blackbody radius, corresponding to the photosphere, expands at a constant veloc-

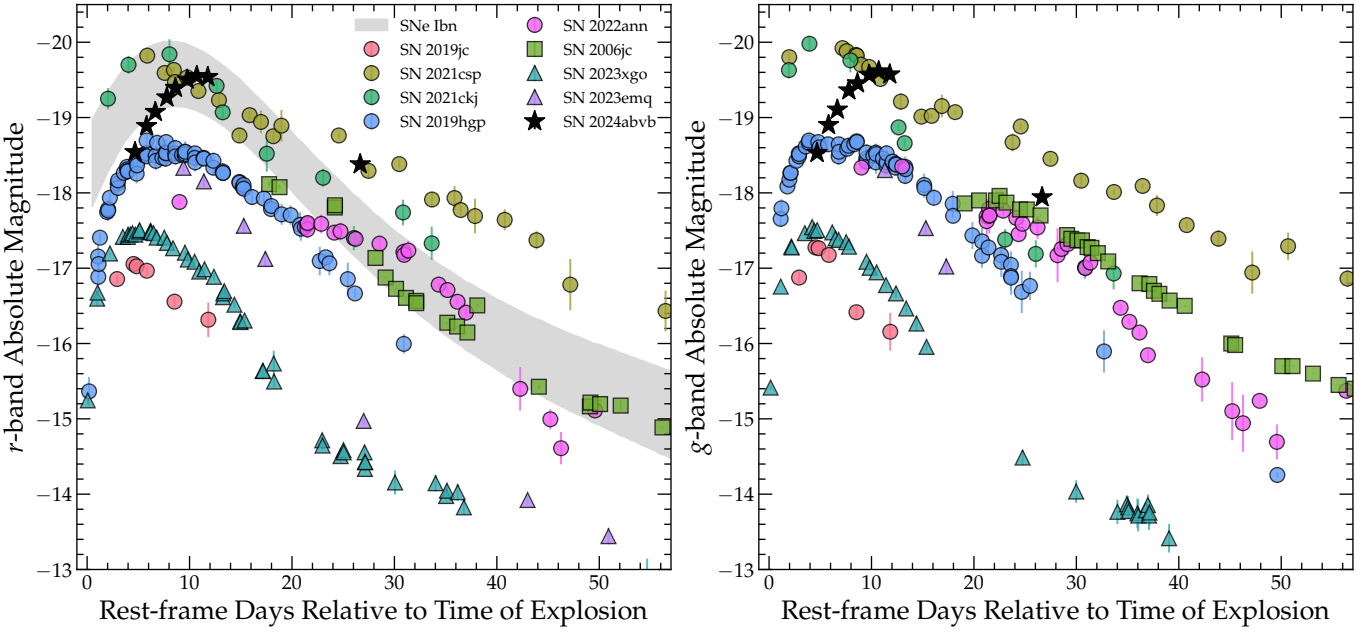


Figure 5. r -band (left) and g -band (right) light-curve comparison of SN 2024abvb with a similar supernovae. Note that since the explosion time for SN 2006jc is not well-constrained, we align the estimated maximum-light epoch from Pastorello et al. (2007) to the maximum of the shaded SNe Ibn template from Hosseinzadeh et al. (2017, shaded grey region). SN 2024abvb exhibits a rapid rise in its early evolution and is among the brightest sources.

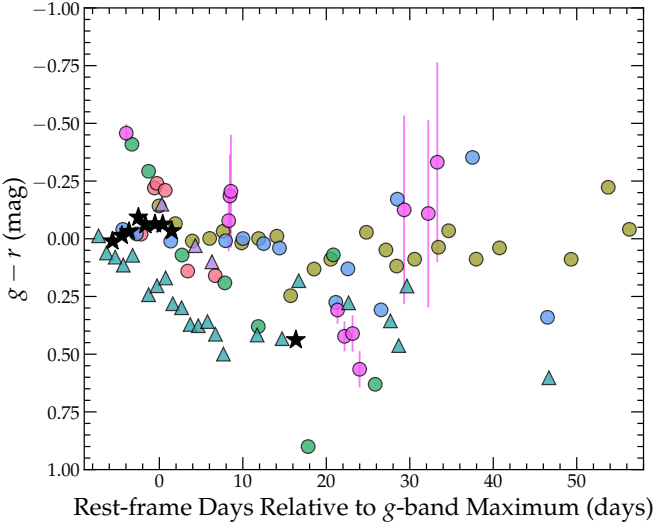


Figure 6. The intrinsic colour evolution ($g - r$) of SN 2024abvb compared to the SNe Icn (Pellegrino et al., 2022b; Davis et al., 2023), transitional SNe Icn/Ibn sample (Gangopadhyay et al., 2025b; Pursiainen et al., 2023). Markers are the same as Figure 5. SN 2024abvb has a colour similar to that of both samples.

ity of $18,600 \text{ km s}^{-1}$, after which it stays constant. However, this value is extremely high, given that the maximum velocity we detect from the spectral features is only 2000 km s^{-1} (see Figure 11), indicating that the spectral features trace the CSM environment.

The temperature evolution of SN 2024abvb is cooler than that of all comparison SNe samples (see the bottom panel of Figure 8). Unlike the majority of interacting SNe that are initially very hot (e.g., $T_{\text{BB}} > 25,000 \text{ K}$ for SN 2022ann),

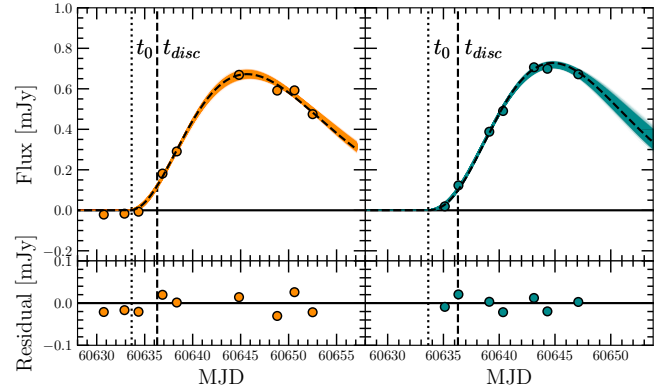


Figure 7. Left: The ATLAS o -band rising light curve. Right: The ATLAS c -band rising light curve. Bottom: The fit residuals. The dotted line indicates the time of first light (t_0) from the best-fit parameters, and the vertical dashed black line indicates the time of discovery (t_{disc}). The dashed black line denotes the best-fit light curve, and the coloured lines represent 1000 randomly sampled light curves from our posterior.

SN 2024abvb has an initial temperature of $\sim 10,500 \text{ K}$. After two days, SN 2024abvb reaches a maximum temperature of $\sim 10,800 \text{ K}$ and cools over the next 45 days. This behaviour contrasts with that of the SNe Icn sample, which show a temperature increase over approximately 5 days before maximum light, followed by a faster subsequent decline. Early-time temperatures for SNe Icn and the transitional candidates decrease from the earliest epochs and begin to plateau around a week after maximum light, cooling more slowly than SN 2024abvb.

In general, the evolution of the blackbody properties is broadly similar to that of the other SNe Icn in our sample, which could suggest that the ejecta and circumstellar environ-

ment of SN 2024abvb is more similar to this population rather than our SNe Icn sample.

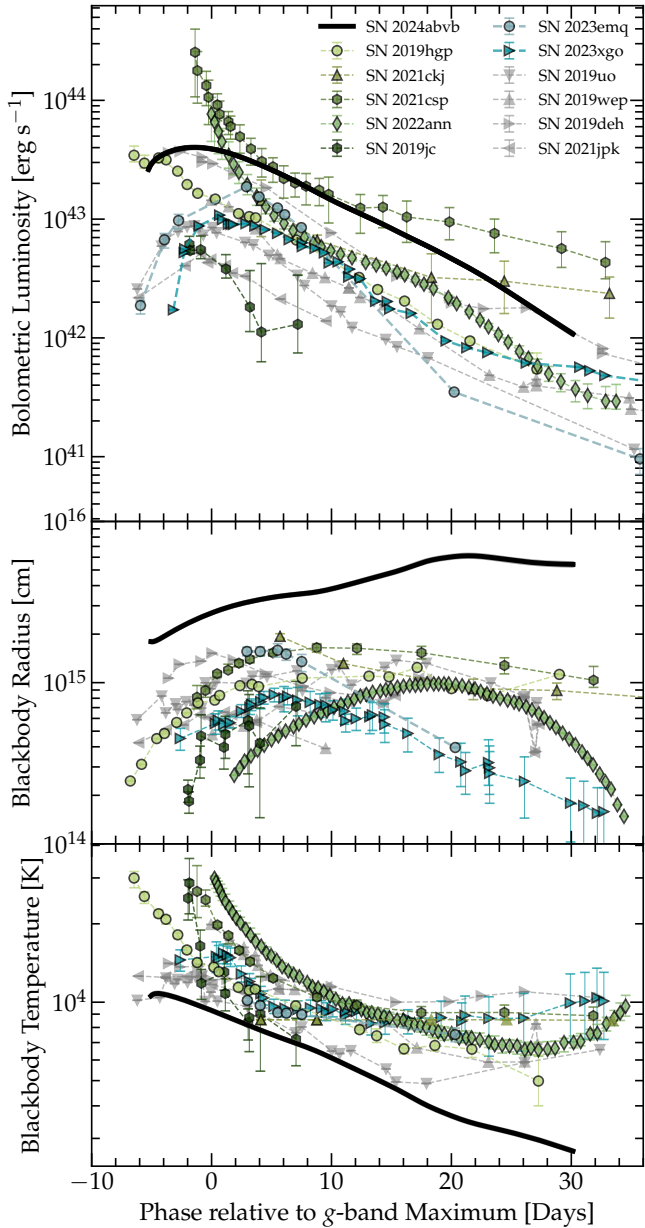


Figure 8. The estimated bolometric light curve (top panel), blackbody radius evolution (middle panel), and blackbody temperature evolution (bottom panel) of SN 2024abvb (black curves with the 1σ uncertainty plotted as a grey band but not visible), a sample of SNe Icn (green markers; Pellegrino et al., 2022b; Perley et al., 2022; Davis et al., 2023), SNe Ibn (grey markers; Pellegrino et al., 2022a), and transitional SNe Ibn/Icn candidates (blue markers; Pursiainen et al., 2023; Gangopadhyay et al., 2025b). Note that SN 2022ann, SN 2021ckj, and SN 2019jc did not have UV observations. The grey shaded band in the top panel is the template light curve of SNe Ibn from Hosseinzadeh et al. (2017). The phase is relative to the g -band maximum. The bolometric luminosity of SN 2024abvb appears consistent with that of the comparison SNe sample; however, it exhibits a significantly larger blackbody radius and a substantially cooler temperature.

3.2.3 Photometric Modelling

The light curves of normal Type Ib and Ic SNe are well-modelled by radioactive ^{56}Ni decay-powered models (e.g., Anderson, 2019). However, this is not always the case for interacting SESNe. The light curves of Type Icn SNe typically require a different and/or additional power source because ^{56}Ni is inconsistent with the photometric properties post maximum light. Additionally, the presence of narrow-line emission in their spectra at early times (see Figure 10), rapid photometric evolution (see Figure 2), high peak bolometric luminosities (see Figure 8), and blue colours (see Figure 6) suggests that CSM interaction is powering the light curve.

However, to investigate whether the light curve is predominantly powered by radioactivity of ^{56}Ni or by a combination of ^{56}Ni decay and CSM interaction, we model the multiband UVOIR light curves of SN 2024abvb using Redback^j (Sarin et al., 2024), a Bayesian inference package for modelling transients. We employ two models: the radioactive decay model from Arnett (1982) (see Appendix 3) and the radioactive decay model with additional CSM interaction from Villar et al. (2017) and Chatzopoulos et al. (2013). The free parameters are inferred using nested sampling with Nestle^k (Barbary, 2021), assuming a Gaussian likelihood.

The presence of narrow C II and O I P Cygni features, together with the bolometric properties, blue colours, and rapid evolution of SN 2024abvb, indicates CSM interaction as the dominant power source. Radioactive decay likely provides an additional contribution, similar to the scenarios proposed by e.g. Perley et al. (2022); Pellegrino et al. (2022b) and Davis et al. (2023). We model this scenario by fitting the multiwavelength light curves with a combination of the Arnett model and the semi-analytical CSM interaction model of Chatzopoulos et al. (2012), implemented as the `csm_nickel` model in Redback. Similar to Pellegrino et al. (2022b), we fixed the optical (electron scattering) opacity to $\kappa_o = 0.04 \text{ cm}^2 \text{ g}^{-1}$, and gamma opacity to $\kappa_\gamma = 0.08 \text{ cm}^2 \text{ g}^{-1}$. The kinetic-to-thermal conversion efficiency, ϵ , is fixed at 0.5 to enable direct comparisons with Pellegrino et al. (2022b) and Davis et al. (2023). The f_{Ni} ($f_{\text{Ni}} = \frac{M_{\text{Ni}}}{M_{\text{ej}}}$) priors were constrained initially to be < 0.008 ($< 0.004 M_{\odot}$), which was taken from the published M_{Ni} values for the SNe Icn sample in Pellegrino et al. (2022b). We assumed that the best-fit value of $< 1 M_{\odot}$ derived from the radioactive decay fit would be outside the fiducial range for CC SNe (see Appendix 3). However, this constraint yielded no fits. Instead, we used broad priors for the nickel fraction, ranging from 0.0001 to 0.50.

Log-uniform priors are adopted for the ejecta mass and CSM mass, motivated by the reported values for the SNe Icn population from Pellegrino et al. (2022b) (see Table 3). A log-uniform prior of $10^{-11} - 10^{-6} \text{ g cm}^{-3}$ is assumed for the CSM density. The inner CSM radius is assigned a uniform prior over $0.1 - 30.0 \text{ au}$, consistent with the range of radii determined by Pellegrino et al. (2022b). The initial prior on η , the CSM

^j<https://redback.readthedocs.io/en/latest/index.html>

^k<http://kylebarbary.com/nestle/>

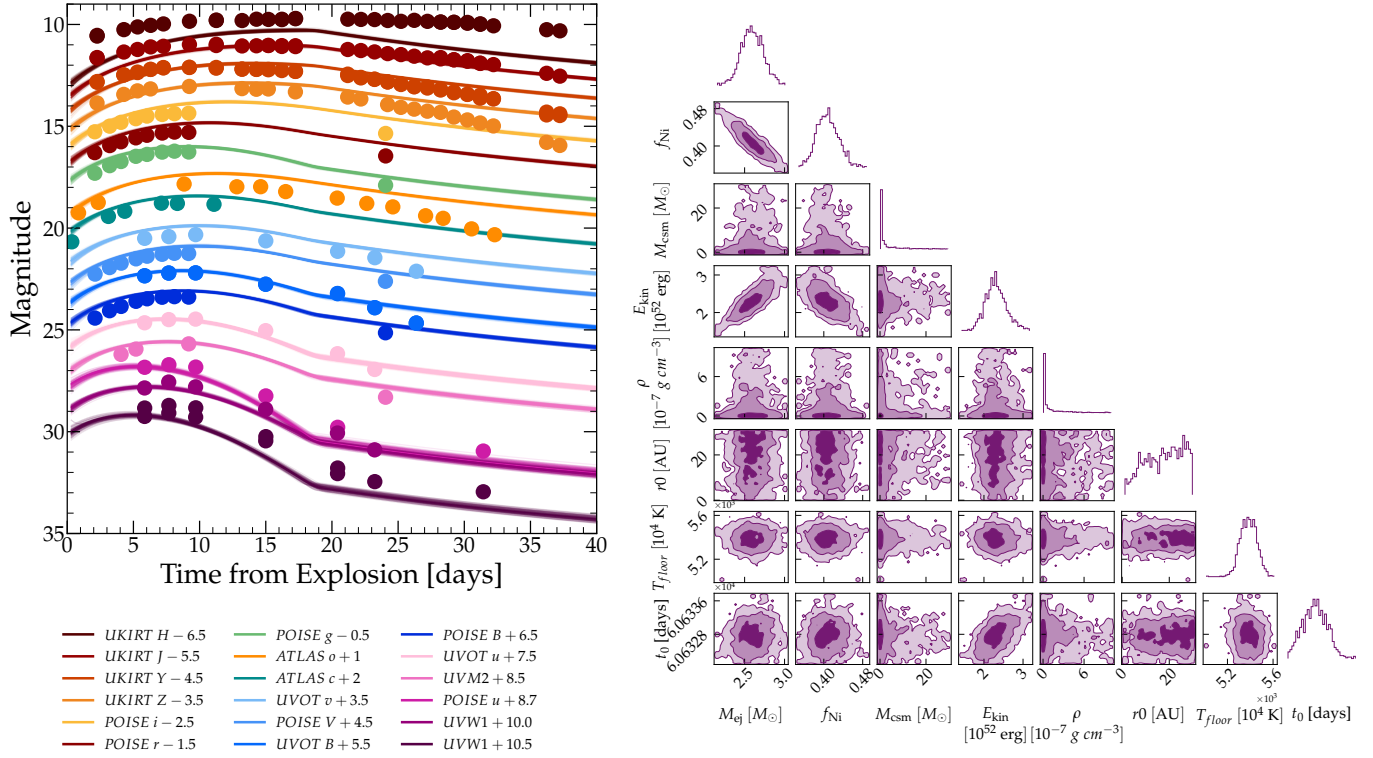


Figure 9. *Left:* The best-fit multi-band light curves of SN 2024abvb using the radioactive decay plus CSM interaction model (Chatzopoulos et al., 2013; Villar et al., 2017). The model exhibits difficulty reproducing the rise to peak in the IR bands and the post-peak decline in the UV bands. *Right:* Corner plot of the model fit to the multi-band light curves of SN 2024abvb computed with Redback. See Table 3 for the best-fit parameters.

density profile index, was chosen as a uniform distribution between $\eta = 0$ (a uniform density CSM shell) and $\eta = 2$ (CSM due to a steady mass-loss wind). The resulting posterior distribution reaches the upper bound of this prior, favouring a wind-like CSM structure for SN 2024abvb. However, to enable comparison with the literature, we fix η to 2, as in e.g., Pellegrino et al. (2022b).

The best-fit light-curve and corner plots are shown in Figure 9, with parameters listed in Table 3. The evolution of SN 2024abvb is consistent with an ejecta mass of $\sim 2.59 M_\odot$ interacting with a CSM mass of $0.28 M_\odot$. Similar to what was found by Fraser et al. (2021) and Pellegrino et al. (2022b), this ejecta mass lies at the upper end of values inferred for other SNe Icn (e.g., $M_{ej} \sim 2 M_\odot$ for SN 2021csp), yet remains below expectations for WR progenitors with pre-SN explosion masses $> 10 M_\odot$. The inferred CSM mass is consistent with that found by Gangopadhyay et al. (2025b) ($\sim 0.22 M_\odot$) for SN 2023xgo and by Pellegrino et al. (2022b) for SN 2019hgp ($\sim 0.26 M_\odot$). However, the posterior for M_{CSM} is weakly constrained compared to other parameters in our analysis (see Figure 9). Consequently, the quoted value should be treated with caution. The inferred ^{56}Ni mass of $\sim 0.1 M_\odot$ exceeds that measured for other SNe Icn by roughly one order of magnitude (e.g., Pellegrino et al. 2022b), but is consistent with values reported for SNe Ibn (e.g., Pellegrino et al. 2024). Maeda & Moriya (2022) found that SNe Ibn produce very little ^{56}Ni mass, with the upper limits $\sim 0.1 M_\odot$, compared to canonical

core-collapse supernovae (CCSNe).

Our fit also yields a CSM mass of $\sim 0.28 M_\odot$ and a CSM radius of ~ 18.5 au. The inferred CSM mass lies within the range reported for SNe Icn, ($0.12 M_\odot < M_{CSM} < 0.73 M_\odot$) whereas the CSM radius is among the highest in the SNe Icn sample, which typically spans 0.05 au $< R_{CSM} < 0.13$ au (Pellegrino et al., 2022b). Pellegrino et al. (2022a) found that the light curves of four SNe Ibn can be reproduced with models featuring ejecta masses of $\approx 1 - 3 M_\odot$, CSM masses of $\approx 0.2 - 1 M_\odot$, and CSM radii of $\approx 20 - 65$ au. However, their derived M_{Ni} is comparable to those reported for SNe Icn. This similarity suggests that SN 2024abvb and SNe Ibn may share a common progenitor system (see Section 4.2).

The best-fit light curve in Figure 9 shows that the CSM+Ni model does not accurately reproduce the rise in the redder IR bands nor the post-peak decline in the UV bands. This suggests that the model may be insufficient to fully capture the behaviour of SN 2024abvb. In particular, the model assumes a uniform CSM density and spherical symmetry, whereas this object may instead feature a clumpy or asymmetric CSM. Gangopadhyay et al. (2025b) applied the same CSM+Ni model implemented in Redback for their transitional candidate, SN 2023xgo, finding ejecta masses, kinetic energy, and CSM radius that are substantially lower than those inferred for SN 2024abvb. They also report difficulty in reproducing the late-time light curve beyond ~ 30 days post-maximum. Similarly, we find that the model struggles to fit the data at phases $\gtrsim 20$ days

post-explosion, indicating that the inferred parameters may be sensitive to the adopted priors, even when these priors are consistent with those in the literature. In particular, the CSM density, radius, and mass are degenerate, so uncertainties in one parameter propagate directly to the others.

Table 3. Best-fit parameters for the Arnett Law plus CSI model. The light curves are well reproduced with a considerably large ejecta mass compared to the SNe Icn and Ibn sample.

Parameters	Priors	Best-Fitted Values
$M_{ej} [M_{\odot}]$	$\log \mathcal{U} [0.1, 30]$	$2.59^{+0.14}_{-0.13}$
f_{Ni}	$\mathcal{U} [0.0001, 0.50]$	$0.41^{+0.02}_{-0.02}$
$M_{csm} [M_{\odot}]$	$\log \mathcal{U} [0.01, 30]$	$0.28^{+4.94}_{-0.25}$
$E_{kin} [\text{erg}]$	$\log \mathcal{U} [5 \times 10^{49}, 5 \times 10^{52}]$	$2.29^{+0.28}_{-0.24} \times 10^{52}$
$\rho [\text{g cm}^{-3}]$	$\log \mathcal{U} [10^{-11}, 10^{-6}]$	$0.14^{+2.56}_{-0.14} \times 10^{-10}$
$r_0 [\text{AU}]$	$\mathcal{U} [1.0, 30]$	$18.50^{+7.99}_{-9.91}$
$T_{\text{floor}} [10^4 \text{K}]$	$\log \mathcal{U} [2 \times 10^3, 10^4]$	$5386.92^{+70.59}_{-73.89}$
$t_0 [\text{days}]$	$\mathcal{U} [t_{\text{exp}} - 2, t_{\text{exp}} + 2]$	$60632.77^{+0.29}_{-0.29}$

3.3 Spectroscopic Properties and evolution

From the ANU 2.3m WiFeS observation taken +1.2 days after peak brightness, a spectrum of the transient and its host galaxy were extracted. As there is no previously known redshift for the host galaxy, the redshift of SN 2024abvb was measured using the automatic redshift software MARZ¹ (Hinton et al., 2016) that matches the input spectrum against galaxy templates. By aligning the narrow H α in the host-galaxy spectrum, a redshift of $z = 0.0391 \pm 0.0002$ was determined. This value is consistent with the redshift provided by the TNS classification of $z = 0.039$ ^m.

The optical spectral sequence of SN 2024abvb is presented in Figure 10. Table A1 presents a log of the spectra. The earliest spectrum of SN 2024abvb at -7.9 d exhibits narrow emission features arising from C, He (and potentially H) that originate from the recombination of the surrounding CSM. These notable features are identified at 3910 Å, 4270 Å, 5890 Å, 6560 Å, and 7230 Å. The first peak is due to a blend of C II $\lambda 3915$ and He I $\lambda 3888$, and the second peak at 4267 Å is due to C II. The third and fifth peaks are a combination of C II and He I lines; the latter peak has a blue wing, while the former is symmetrical. The fourth peak is dominated by C II emission, with likely weak H α contribution due to the proximity of the neighbouring H α line. Overall, the narrow-line features are seen until 7.2 days after maximum light.

In addition, there is a weak O I $\lambda 7774$ P Cygni line that gradually strengthens $\sim 7 - 22$ days after maximum light.

Additionally, we see emission signatures from the Mg II $\lambda 4481$, $\lambda 7877$, $\lambda 7896$ lines, and weak Ca II triplet lines. The Mg II $\lambda 4481$ emission line is also observed in some SNe Ibn (SNe Icn) such as SN 2006jc (Pastorello et al., 2007) and SN 2019hgp (Pellegrino et al., 2022b). The early presence of Mg lines suggests that the outer H and He shells of the progenitor have been stripped via stellar winds or binary interaction, which exposes the deeper O-Mg layer (Kuncarayakti et al., 2022).

Several He features are present in the first two spectra of SN 2024abvb (-7.9 d and -4.9 d prior to peak brightness). In the forest of highly ionised lines blueward of ~ 5400 Å, narrow He I emission lines at $\lambda 4922$ and $\lambda 5015$ fade by the third spectrum (-3.4 d). It is difficult to discern whether He I $\lambda 5876$ is a strong feature since it is coincident with the strong C II $\lambda 5890$ line. He I $\lambda 7065$ and $\lambda 7281$ emission is also identified on the blue and red wings of C II $\lambda 7234$ during the first four spectra, but disappears by +1.6 days after peak.

From +4.2 days until +15.2 days, the C II $\lambda 7234$ line has evolved to an absorption line. However, this absorption feature disappears at +17.9 days. Between +4.2 days and +7.2 days, the narrow He I and He II emission transitions to absorption features. At the latter phase, He I $\lambda 4922$, $\lambda 5015$ absorption lines appear and continue to strengthen until +21.9 days. From 15.2 days after peak brightness, we see a gradual strengthening of He I $\lambda 5875$ and O I $\lambda 7774$ P Cygni lines.

Figure 11 shows the isolation of C II; $\lambda 4265$, $\lambda 5890$, $\lambda 6583$, and $\lambda 7234$. The early evolution of C II $\lambda 5890$ and C II $\lambda 7234$ exhibits roughly symmetrical line profiles. At the time of strongest emission, the velocity for each line varies from about 2200 km s^{-1} to 900 km s^{-1} . At +8.8 days, absorption features emerge, with C II $\lambda 5890$ evolving into a P Cygni feature. The C II $\lambda 5890$ and C II $\lambda 6583$ lines are likely blended with He I $\lambda 5876$ and H α $\lambda 6562$, respectively, which may alter the line profile. The spectral evolution of C II $\lambda 5890$ and C II $\lambda 6583$ is similar to that of SN 2022ann at comparable epochs (see Figure 9 in Davis et al. 2023).

In Figure 12 we show the pseudo-equivalent widths (pEWs) of the C III emission at 5700 Å for the early spectra of SN Ibn, SN Icn, and transitional Ibn/Icn candidates compared with SN 2024abvb. The C III 5700 Å emission in SN 2024abvb is the weakest among the sample; with estimated pEW values of 0.12 ± 0.53 Å and 0.80 ± 0.30 Å at -7.9 d and -4.9 d relative to peak brightness, respectively. These values are approximately an order of magnitude smaller than those measured for SNe Ibn, and about two orders of magnitude smaller than the pEWs observed in SNe Icn. The weakness of C III suggests that the emitting region lacks carbon and has low ionisation conditions.

3.3.1 Pre-Peak Optical Spectral Evolution

We compare the spectra of SN 2024abvb with a sample of SNe Ibn, Icn, and transitional Ibn/Icn, which show signatures of narrow-line features in their early spectra. For the SNe Ibn (blue spectra), the following objects were selected: PS1-12sk (Sanders et al., 2013) and SN 2024acyl (Dong et al., 2025),

¹<https://samreay.github.io/Marz/>

^m<https://www.wis-tns.org/object/2024abvb>

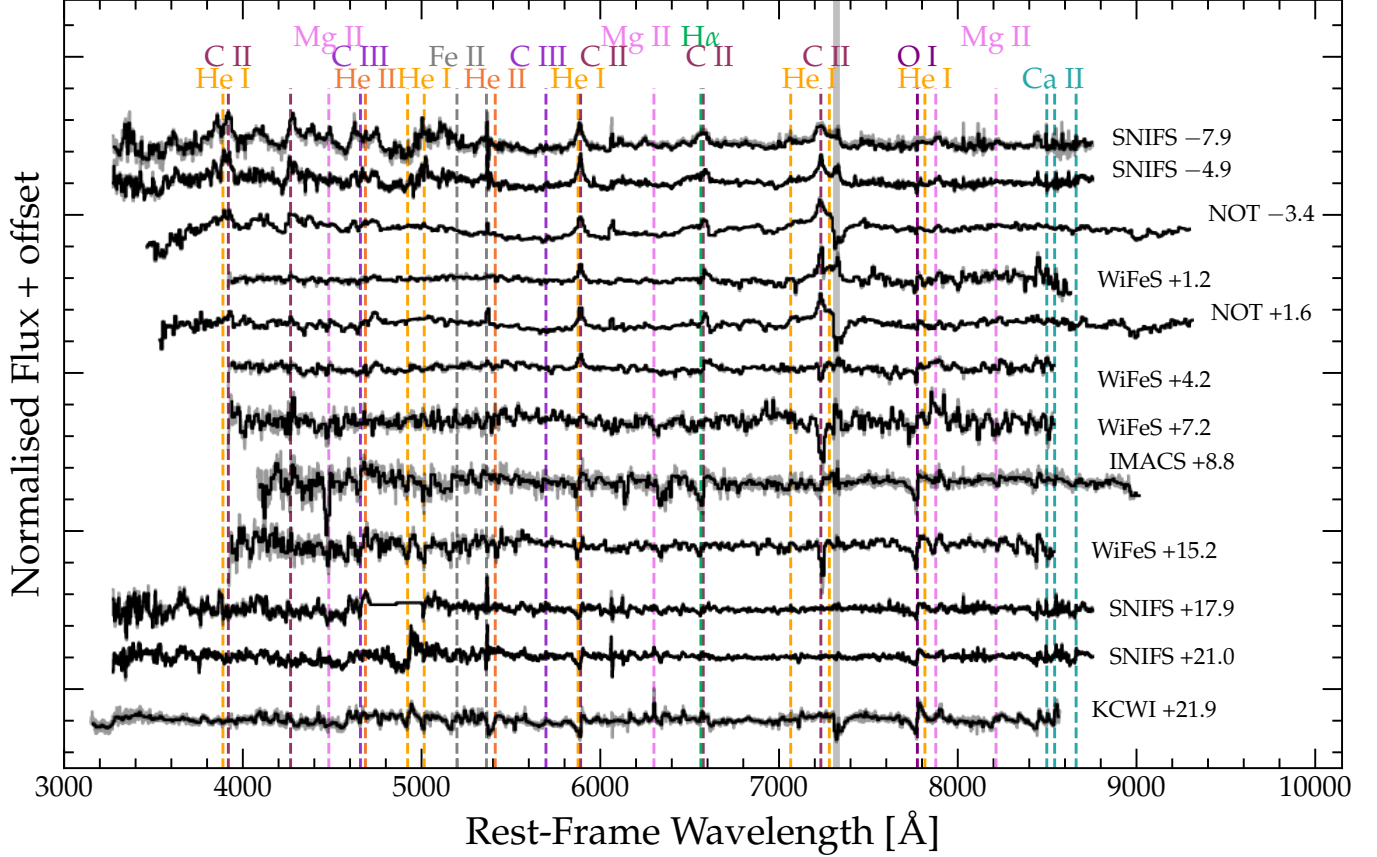


Figure 10. The optical spectral timeseries of SN 2024abvb. All fluxes have been normalised and vertically offset for clarity. The data has been binned into 5 \AA -wide bins from the original observations. Phases are calculated relative to the α -band maximum light on MJD 60645.27. Dashed lines correspond to prominent emission features. The grey shaded region indicates telluric absorption bands.

the only SNe Ibn with projected distances larger than that of SN 2024abvb (see Section 3.1); SN 2022pda (Fulton et al., 2022), which has an early pre-peak spectrum obtained at a phase similar to the first spectrum of SN 2024abvb. The sample also includes SN 2023ubp (Tonry et al., 2023; Hinkle, 2023), SN 2022ablq (Pellegrino et al., 2024), SN 2023tsz (Warwick et al., 2025); which exhibit C II emission similar to that of SN 2024abvb at comparable phases, and SN 2006jc (Pastorello et al., 2007); the prototypical SN Ibn. Among the SNe Icn (green spectra), we compared SN 2024abvb with SN 2019hgp, SN 2019jc, SN 2021csp, SN 2021ckj, and SN 2022ann. We also included the only two transitional Ibn/Icn SNe (pink spectra) found in the literature: SN 2023emq and SN 2023xgo. All the comparison spectra were downloaded from WISEREP (Yaron & Gal-Yam, 2012) and corrected for the host-galaxy redshift.

In Figure 13, we compare the early-time optical spectra of SN 2024abvb with the aforementioned SNe sample. The first spectrum of SN 2024abvb was obtained ~ 8 days before maximum, making it one of the earliest epochs in our sample of interacting SNe, second to only SN 2022pda. Compared to SN 2022pda, both SNe show strong C II lines and exhibit a hot blue continuum. All the SNe Icn spectra exhibit C III emission features at 4658 \AA and 5696 \AA , which are typical features seen

in the SNe Icn sample in Pellegrino et al. (2022b). The 5696 \AA emission is present in SN 2023emq but is weaker than the SNe Icn, SN 2019hgp, and SN 2019jc. These emission features are extremely faint in SN 2024abvb. Instead, we see strong peaks of C II blended with He I at 5890 \AA and 7230 \AA , which are two of the most prominent emission lines in SN 2024abvb that are not observed (or rather very faint as for SN 2019hgp at -3.4 days (5890 \AA) and SN 2019hgp (7230 \AA) in the SNe Icn sample.

A notable feature seen in the very early spectra of SN 2024abvb is the lack of C III emission at ~ 5700 \AA compared to other SNe. C III 5696 \AA is the most prominent in SNe Icn and SNe Ibn/Icn, but is not seen in SN 2024abvb and SNe Ibn: SN 2022pda and SN 2023ubp. SN 2024abvb also shares similar C II emission features with our SNe Ibn sample. Both SNe Ibn spectra contain strong C II emission features at 5890 \AA , 6583 \AA , and 7234 \AA , which is also seen in SN 2024abvb.

Ne is rarely seen in CCSNe spectra (Pellegrino et al., 2022b). Yet in Figure 13, we see Ne II features in the early time spectra of SN 2024abvb and Icn SNe 2019jc and 2019hgp (Gal-Yam et al., 2022). In particular, the first two spectra of SN 2024abvb display strong Ne II $\lambda 3933$ and $\lambda 4607$ features. Pellegrino et al. (2022b) suggest that this Ne originates from

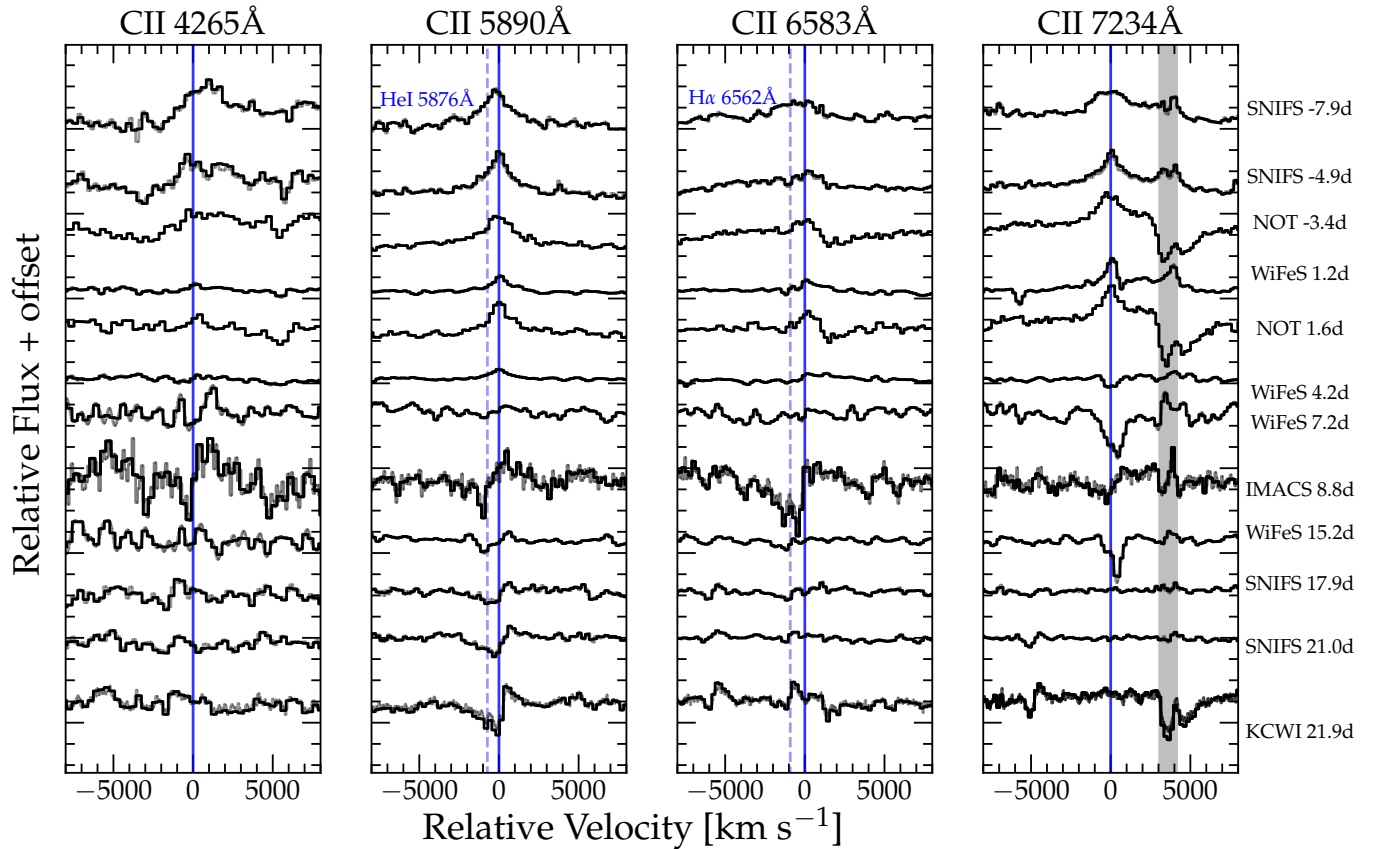


Figure 11. Evolution of the C II features in 2024abvb. We plot 4265 Å, 5890 Å, 6583 Å, and 7234 Å on a velocity scale relative to their respective rest wavelengths marked by blue solid lines. The blue dashed lines show neighbouring features that blend with the main line profile. Continuum-subtracted spectra plotted in black and binned into 5 Å-wide bins, while the light grey spectra are the original data. The phases relative to the α -band maximum light and the respective instrument are shown on the right.

C-burning and was stripped from the inner layers of the progenitor. As such, measuring the Ne abundance in the CSM could help constrain progenitor channels.

The spectroscopic sequence at peak brightness (from -1.4 to $+5$ days) in Figure 14, shows that SN 2024abvb is highly similar to SNe Ibn 2023tsz and SN Icn 2022ann. SN 2024abvb, like other SNe Icn lacks He I and He II features. Unlike some SNe Icn, it shows no early significant P Cygni absorption blueward of 5000 Å or C III emission (see Pellegrino et al. 2022b). Instead, C II features dominate, notably a strong 7234 Å and a weaker 6583 Å, line, similar to SN Icn 2022ann. SN 2022ann also does not exhibit strong C III lines which are seen in SN Icn 2021csp or 2019jc. SN 2024abvb does not show any broad He I and He II emission lines like in SNe Ibn 2022ablq, but rather weak He lines like in SN 2023tsz. However, the C II features present in these SNe are alike. In this case, SN 2024abvb has features most consistent with SN 2023tsz from the SNe Ibn sample and SN 2022ann from the SNe Icn sample.

3.3.2 Post-Peak Optical Spectral Evolution

In Figure 15, the spectral behaviour of SN 2024abvb diverges from the typical behaviour of SNe Ibn at late times. From $+7.2$

days post peak, the strong C II features have faded and P Cygni features have developed in SN 2024abvb. Apart from the C II P Cygni features (see Figure 11) we also see a O I 7774 Å P-Cygni line emerging, which is consistent with SNe Icn (Pellegrino et al., 2022b). At this epoch, SN 2024abvb more closely resembles SNe Icn 2019hgp and 2021csp. For the SNe Ibn (SN 2006jc and PS1-12sk), broad intermediate-width lines can be seen at He I 5876 Å and O I 7774 Å. However, we do not observe broad He I emission lines in SN 2024abvb but rather small absorption dips at 4922 Å and 5015 Å. Starting around 19 days after peak brightness, the strongest features in SN 2024abvb are the O I and C II P Cygni lines, coinciding with the onset of light-curve decline. At a similar phase, SN 2022ann (Davis et al., 2023) also exhibits these P Cygni features. However, by about 60 days after peak, they transition to forbidden emission lines, indicating a shift to the nebular phase. Our dataset is limited to the photospheric phase, so we are unable to detect potential forbidden emission lines.

Pellegrino et al. (2022b), and Perley et al. (2022) report a transition from a narrow-line phase to a broad-line phase in their spectra. For example, Pellegrino et al. (2022b) highlight that around 3 weeks after maximum light, broad spectral features (with velocities of $\sim 10,000 \text{ km s}^{-1}$) start to emerge (e.g., a broad Ca II NIR triplet in SN 2021csp). On the other hand,

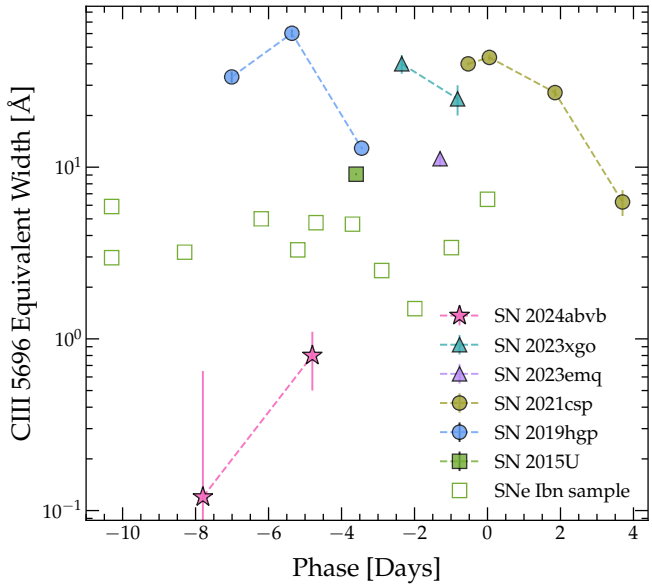


Figure 12. Pseudo equivalent width measurements of the C III 5700Å emission for SN 2024abvb (pink star), SNe Icn 2021csp and 2019hgp (green and blue circles), SNe Ibn/Icn candidates 2023emq and 2023xgo (purple and teal triangles), and flash-ionised SNe Ibn (green squares). Open green squares indicate 3σ upper limits for SNe Ibn with ambiguous C III detections (see Figure 5 from Pursiainen et al. 2023). Phases are relative to the r -band maximum light. SN 2024abvb does not resemble any comparison sample.

SN 2019hgp maintains its narrow features for longer than SN 2021csp but eventually develops broad P Cygni features. Gangopadhyay et al. (2025b) also identified this transition in SN 2023xgo, but for the He I 5876 Å line and suggest the broad features are a signature of the SN ejecta while the narrow features arise from the undisturbed He-rich CSM. However, like SN 2022ann, such a transition is not present in SN 2024abvb; the narrow Ca II NIR triplet persists and only slightly strengthens ~ 15 days after peak. We were unable to obtain subsequent optical spectroscopy to search further for broad lines because SN 2024abvb became too faint before such lines emerged.

3.3.3 Near Infrared Spectrum

Figure 16 presents the NIR spectra. One week after maximum light, the SED is dominated by a strong blue continuum. In the spectrum taken at +6.8 days, searches for He I, C I, and O I NIR features commonly seen in SESNe (Shahbandeh et al., 2022) reveal no strong 1.08 μm He I line (seen in 2023emq; Pursiainen et al. 2023 and SN 2022ann Davis et al. 2023) nor the 1.13 μm O I line. We identify tentative 1.07 and 1.18 μm C I lines. In the spectrum taken at +16.9 days, weak 1.08 μm He I, 1.07 μm, and 1.18 μm C I lines are present. The contemporaneous optical spectrum (+17.9 days; SNIFS) also exhibits weak He lines. At a similar epoch, strong 1.06 μm C I emission was detected in the Type Icn SN 2021csp (Fraser et al., 2021).

4. Discussion

Our photometric and spectroscopic analysis indicates that SN 2024abvb is not strictly a Type Icn SN. We now synthesise the evidence to evaluate whether it more closely resembles a Type Ibn or Type Icn event. In this section, we also estimate the local SFR properties and present possible progenitor channels that could potentially explain the unique characteristics of SN 2024abvb.

4.1 Host-Galaxy Offset

One of the most striking characteristics of SN 2024abvb is its projected offset from its host galaxy. In Section 3.1, we found that SN 2024abvb has the largest offset (22.4 kpc) from its host-galaxy compared to other SNe Icn in our sample (and the third largest among the SNe Ibn sample). However, the question arises as to how SN 2024abvb arrived at its explosion site, assuming its progenitor originated from its host galaxy.

Explaining the large offset of SN 2024abvb remains challenging. As a quick estimate, if the progenitor of SN 2024abvb was a single star with a zero-age main-sequence (ZAMS) mass of $M_{\text{ZAMS}} = 8 M_{\odot}$ and a lifetime of ≈ 50 Myr (see Figure 3. in Zapartas et al. 2017), it would require a velocity of ~ 780 km s $^{-1}$ to move 22.4 kpc during that time. On the other hand, if we assume the progenitor of SN 2024abvb is towards the higher mass limit, a $M_{\text{ZAMS}} = 40 M_{\odot}$ star with a lifetime of ≈ 7 Myr, this would require a velocity of ~ 3100 km s $^{-1}$. Such an extreme velocity is highly unlikely, given that it exceeds the velocity achievable through the Hills mechanism, and the fastest observed unbound main-sequence stars (hypervelocity stars) reach only ~ 1000 km s $^{-1}$ (Brown, 2015; Kreuzer et al., 2020). These considerations suggest that the progenitor would more likely be a lower mass progenitor. A binary progenitor scenario is appealing because it allows for a lower-mass star; however, achieving near 1000 km s $^{-1}$ in a binary system is difficult.

For the same upper mass-limit assumption ($M_{\text{ZAMS}} = 40 M_{\odot}$), Hosseinzadeh et al. (2019) estimated that SN 2006jc, the only SN Ibn with a direct progenitor detection during an outburst, would require a velocity of >530 km s $^{-1}$ to reach its terminal location, substantially lower than the velocity required for SN 2024abvb. SN 2019jc has a projected offset of 11.2 kpc which is the second largest in the SNe Icn sample. Pellegrino et al. (2022b) conservatively estimated that a runaway velocity of ≈ 250 km s $^{-1}$, which is of the same order of magnitude as our estimate for a $M_{\text{ZAMS}} = 8 M_{\odot}$ progenitor, would be required for SN 2019jc to reach its explosion site within its lifetime. They further noted that if SN 2019jc originated from a WR star in a binary system, such a velocity is an order of magnitude lower than typical kick velocities imparted by companion SNe (Renzo et al., 2019), and that most massive stars at most travel hundreds of parsecs before exploding (Eldridge et al., 2011). Although, Pellegrino et al. (2022b) suggested that such runaway velocities could be achieved through interactions with stellar clusters, the location of SN 2024abvb is devoid of star formation (see Section 4.3). We therefore tentatively rule

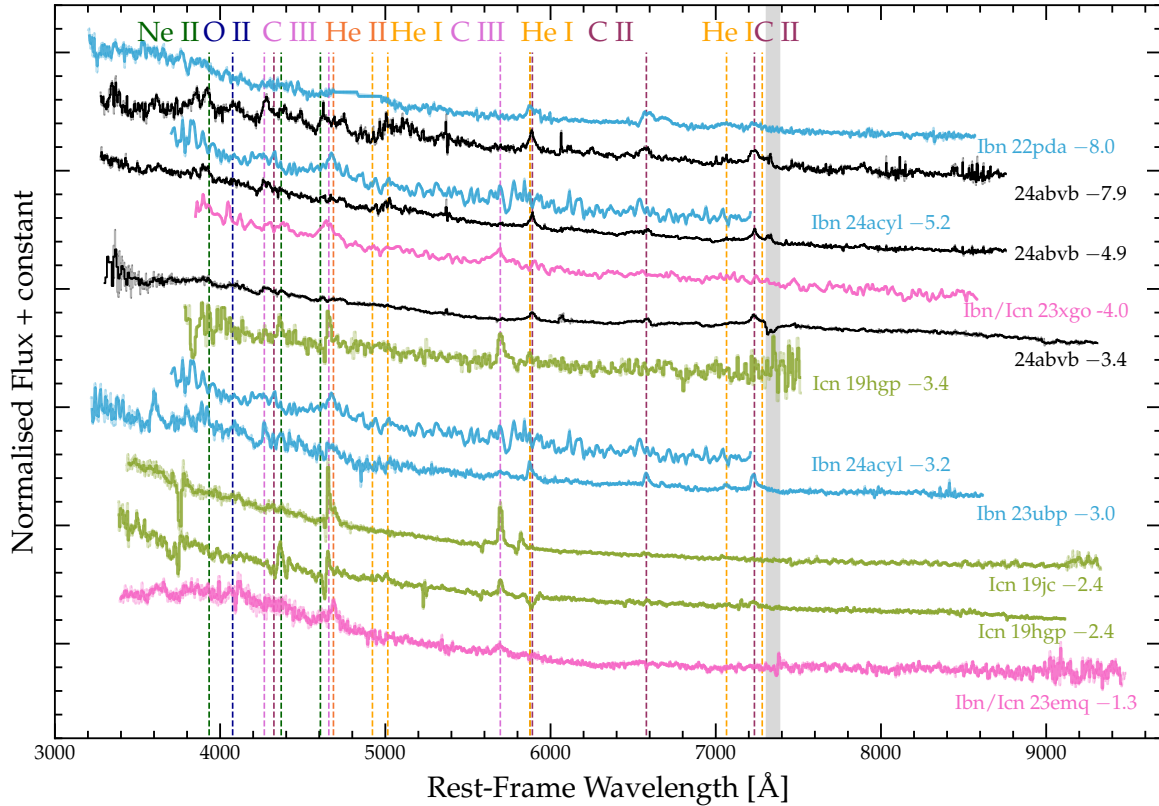


Figure 13. Comparison of SN 2024abvb spectra with Type Ibn (blue), Icn (green), and Ibn/Icn SNe events (pink) at pre-peak epochs. The prominent spectral lines are marked, and the indicated phases are relative to the maximum light. All spectra are binned into 5 Å-wide bins from the original data. The grey shaded regions indicate telluric absorption bands.

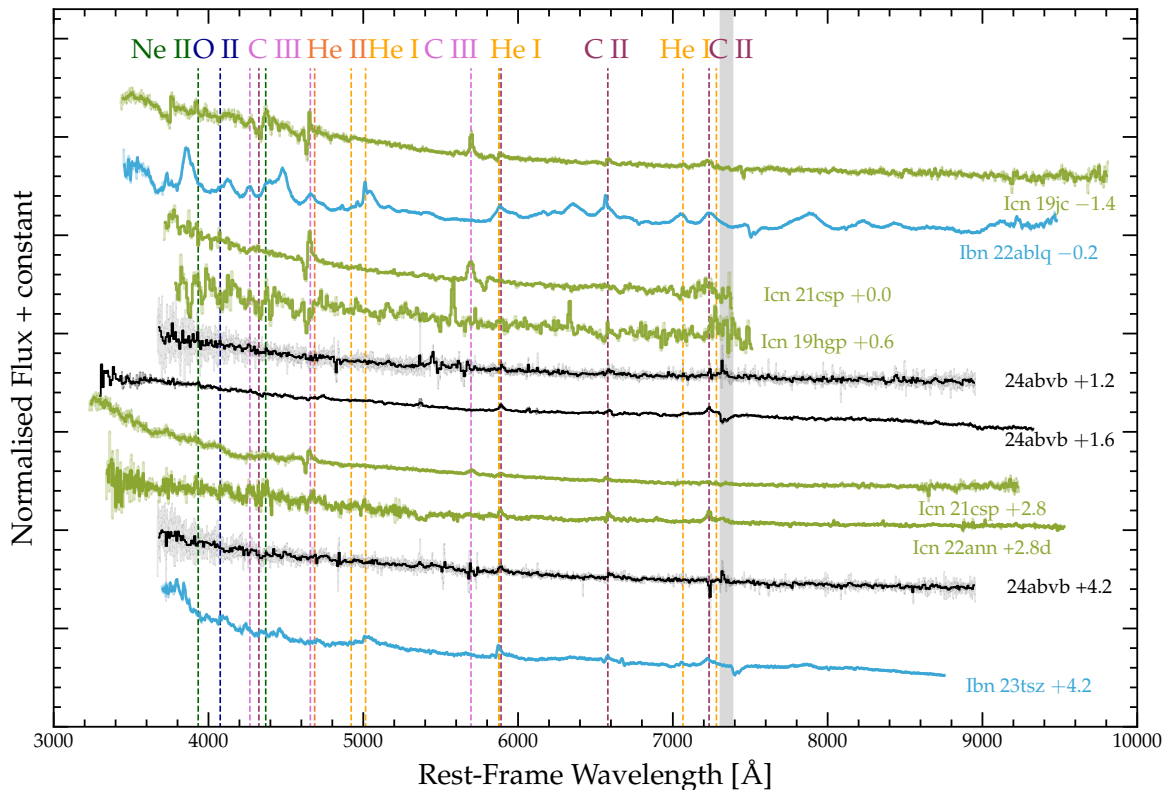


Figure 14. The spectral evolution of SN 2024abvb near peak-brightness (-1.4 to +5 days) compared with SNe Icn (green) and Ibn (blue). SN 2024abvb shows C II features similar to SN 2022ann and SN 2023tsz.

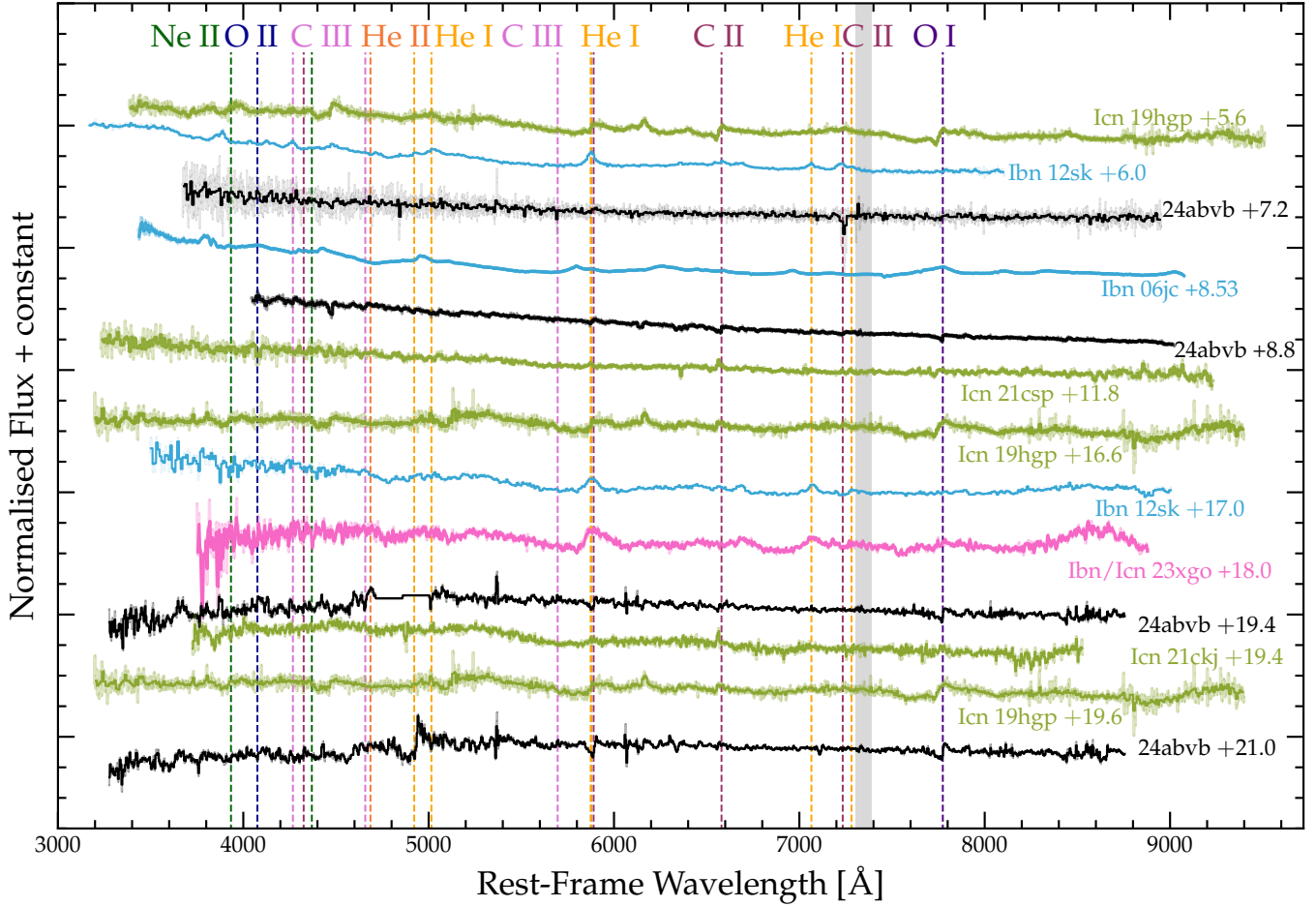


Figure 15. Post-peak spectral evolution of SN 2024abvb compared with Type Ibn (blue), Icn (green), and transitional Ibn/Icn (pink) events. Unlike the SNe Ibn, SN 2024abvb shows no broad He emission at this phase, instead exhibiting strong C II and O I P Cygni features similar to the Type Icn SN 2019hgp.

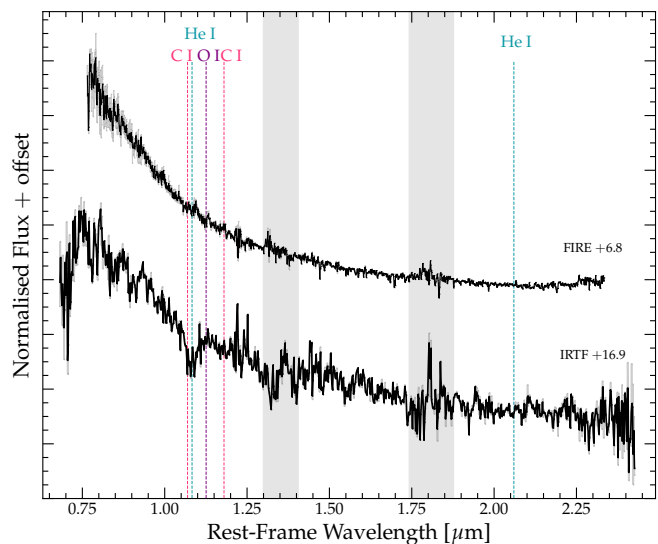


Figure 16. NIR spectra for SN 2024abvb. Each spectrum is binned from the original data into 10 Å-wide bins. Phases are relative to α -band maximum light. Dashed lines correspond to spectral features seen in other SNe Icn NIR spectra. Grey shading denotes the telluric regions.

out a (high-mass) WR star progenitor for SN 2024abvb. It is also important to note that the measured offset is a projected distance, so the true physical separation is likely larger, making these velocity estimates lower limits.

4.2 SN 2024abvb: Ibn or Icn?

4.2.1 Considerations for a SN Ibn

Even though SN 2024abvb was spectroscopically classified as a Type Icn after peak, it exhibits photometric and spectroscopic properties similar to those of SNe Ibn. For example, the bolometric luminosity evolution and peak r -band magnitude match the SNe Ibn template from Hosseinzadeh et al. (2017) (see Figure 8 upper panel, grey band). Turning to the spectra, the early phase of SN 2024abvb could lead to a classification as a SN Ibn due to the abundance of C II lines and lack of prominent C III features, although early emission of C III $\lambda 5700$ has been observed in SNe Ibn (e.g., SN 2023emq (Pursiainen et al., 2023) and 7 others in the SNe Ibn sample from Farias et al. (2025)). While the presence of C emission does not determine whether a SN is classified as a SN Ibn or SN Icn, it is interesting to note that early C II emission is

generally more prevalent in SNe Ibn, whereas C III is more common in SNe Icn. Generally, the detection of C II and C III lines suggests C-rich outer layers in the progenitor star. Since C III requires a higher ionisation potential than C II, its presence implies hotter ejecta, whereas C II emission may indicate carbon-rich, and potentially hydrogen-rich, CSM, possibly arising from episodic mass loss prior to explosion. By day 4 post-explosion, SN 2024abvb is not dominated by strong narrow He I lines, unlike the SNe Ibn at similar phases. As such, based on its early-time spectra (-7.9 to -3.4 days relative to peak light) SN 2024abvb shows similarities to SNe Ibn.

The inferred blackbody and CSM properties of SN 2024abvb are broadly consistent with those of the SNe Ibn population. Its initial blackbody temperature, for instance, closely matches those of SNe Ibn (see the bottom panel of Figure 8). Farias et al. (2025) found that a sub-sample of SNe Ibn exhibit a wide range of CSM masses ($\sim 0.01 - 1 M_{\odot}$) and ejecta masses ($\sim 0.1 - 10 M_{\odot}$), suggesting that many originate from a binary progenitor system. However, massive He-rich WR stars remain viable progenitors for SNe Ibn with very high ejecta masses ($\sim 10 M_{\odot}$), indicating there are multiple progenitor channels. Given that SN 2024abvb is photometrically similar to SNe Ibn at early times, its pre-explosion progenitor and mass-loss mechanism may plausibly have been similar. The derived ejecta and CSM masses for SN 2024abvb ($2.59 M_{\odot}$ and $0.3 M_{\odot}$, respectively) are consistent with those of SNe Ibn. However, the derived nickel mass is an order of magnitude higher than those reported in Farias et al. (2025). Despite this, a binary system still remains a possible explanation for its progenitor system or at the very least a heavily stripped star exploding in a dense H/He-poor and C-rich CSM.

4.2.2 Considerations for a SN Icn

The strong photometric diversity of SNe Icn (Pellegrino et al., 2022b; Davis et al., 2023) indicates that SN 2024abvb falls within the observed range for this class. The six known SNe Icn span a wide range of peak bolometric luminosities ($0.6 - 3 \times 10^{44} \text{ erg s}^{-1}$) (top panel in Figure 8) and SN 2024abvb has a peak luminosity comparable to that of SN 2019hgp and a similar post-peak evolution to SN 2022ann. The early light-curve evolution (Figure 5) among SNe Icn is also diverse, with SN 2021csp showing a fast post-peak decline, while SN 2022ann fades more gradually. The light curve behaviour of SN 2024abvb falls well within this observed range. Additionally, SN 2024abvb maintains an approximately constant $g - r \approx 0$ colour during the first 10 days after maximum light, consistent with most of the SNe Icn sample that have well-sampled colour coverage, such as SN 2019hgp and SN 2021csp.

Near maximum light, SN 2024abvb displays spectral features similar to those of SNe Icn. Its optical spectra $+1.2$ days after peak lack H and He I emission and show narrow C II P Cygni lines, matching SN 2012csp and SN 2022ann. These features suggest that SNe Icn have similar composition and C-rich and H/He-poor circumstellar environments. In addition, SN 2024abvb, like SN 2022ann, shows no broad features after peak light or once the narrow emission lines begin to

fade. Davis et al. (2023) attribute this to either a very low explosion velocity ($\sim 800 \text{ km s}^{-1}$) or obscured SN ejecta. The low-velocity scenario is favoured here, as we see evidence of ongoing CSI with a C-rich CSM in our spectra.

Based on its optical spectra, SN 2024abvb cannot strictly be classified as a SNe Ibn or SNe Icn. Although it shows early-time similarities to flash-ionised SNe Ibn, the presence of strong C II features, and the absence of He I emission at late times suggest that it is best interpreted as a SN Icn with SN Ibn-like characteristics. Placing SN 2024abvb in the context of transitional SN Ibn/Icn events, we favour interpreting it as a transition from SN Ibn to SN Icn. If so, SN 2024abvb would represent the first example of such a transitional event, noting that Pursiainen et al. (2023) and Gangopadhyay et al. (2025b) previously suggested SN 2023emq and SN 2023xgo, respectively, may represent the opposite transition.

4.3 Local environment and implications for the progenitor

To characterise the local environment of SN 2024abvb, we follow the methodology of Sand et al. (2018, 2021) to constrain the local SFR. Because SN 2024abvb is well separated from its host galaxy, the properties of the local stellar environment may provide important insights into the final stages of the progenitor system prior to explosion. A careful examination of Figure 10 shows no H emission features. As such, we constrain the SFR of the local environment by estimating the maximum H α emission using the flux-calibrated and redshift-corrected late-phase spectrum obtained at $+21.9$ d relative to the o -band maximum (see Figure 10). Previous works have predicted that if a SN progenitor system contains a non-degenerate companion star, interaction between the SN ejecta and the companion would produce narrow H emission lines with $\text{FWHM} \approx 1000 \text{ km s}^{-1}$ at late times (Botyánszki et al., 2018; Tucker et al., 2020, and others). We note that this approach entails systematic uncertainties; a more detailed treatment would require assumptions about the companion star type and, more challenging, the explosion energy and binary separation, which are beyond the scope of this work.

Here, we set a quantitative limit on the maximum H α emission by implanting a synthetic emission line into our data. First, we bin the flux-calibrated and redshift-corrected spectrum to the spectral resolution of the data, $\sigma \approx 5 \text{ \AA}$. This resolution is calculated from using the red channel grating with the medium slicer ($R \sim 1800$) and a central wavelength, $\lambda \approx 7150$. Note that Sand et al. (2021, 2018) used a nebular phase spectrum for their analysis, but since SN 2024abvb faded well before it reached the nebular phase, we use the last spectrum in our dataset (i.e., KCWI spectrum at $+21.9$ d). We then employ a second-order Savitsky-Golay filter with a width of 180 \AA to smooth the spectrum on scales greater than the expected emission ($\text{FWHM} \approx 1000 \text{ km s}^{-1}$) in order to determine the continuum around the H α line wavelengths. This width was chosen as we found that smaller widths prevented us from detecting and measuring the implanted faint

$H\alpha$ emission feature. The synthetic $H\alpha$ emission is measured from the residual spectrum, which is the difference between the smoothed and original spectrum. We assume a line width of $\text{FWHM} \approx 1000 \text{ km s}^{-1}$ and a peak flux that is four times the root mean square of the residual spectrum to be the maximum parameters for the implanted $H\alpha$ Gaussian feature to remain undetected. We obtain a 1σ upper limit of the $H\alpha$ flux of $1.58 \times 10^{-16} \text{ erg s}^{-1} \text{ cm}^{-2}$, which has the luminosity limit of $5.63 \times 10^{38} \text{ erg s}^{-1}$ at a distance of 172 Mpc.

We also use the derived $H\alpha$ flux to trace the ongoing star-formation history (<16 Myr old) of the local environment (Gogarten et al., 2009; Dastidar et al., 2025). We employ Equation 2 from Kennicutt (1998), which relates the $H\alpha$ luminosity to the SFR and the scaling factor (0.63) from Madau & Dickinson (2014), to convert from the Salpeter IMF to the Chabrier IMF. From this, we calculate a local SFR limit of $0.0028 \text{ M}_\odot \text{ yr}^{-1}$. This value is significantly smaller than the global SFR, i.e. $0.10 \text{ M}_\odot \text{ yr}^{-1}$ (see Section 3.1), which is not surprising given the extreme offset between SN 2024abvb and its host galaxy. We note that this local SFR is consistent with two SNe Ibn found highly offset from their host-galaxy: SN 2023tsz (Warwick et al., 2025) and PS1-12sk (Sanders et al., 2013). For SN 2023tsz, Warwick et al. (2025) do not rule out a single stripped star progenitor given the exceptionally low SFR of the environment, and Hosseinzadeh et al. (2017) propose that the progenitor of PS1-12sk could be a massive star ejected or tidally stripped from a nearby ultra-compact dwarf galaxy. If an ultra-compact dwarf galaxy is present near SN 2024abvb, it would be extremely faint as pre-explosion images (limiting magnitude of ~ 20 mag in Swope r -band observations Coulter et al., 2017) show no signs of any galaxies at the SN location.

Additionally, we calculate the local SFR density. The KCWI spectrum was extracted using an aperture with a radius of $0.294''$, corresponding to a physical radius of 0.245 kpc. This aperture subtends an area of 0.19 kpc^2 and, when combined with the SFR upper limit derived above, yields a SFR density of $1.5 \times 10^{-2} \text{ M}_\odot \text{ yr}^{-1} \text{ kpc}^{-2}$. Comparing our inferred SFR density with those of SNe Ibn and SNe IIn at the explosion sites presented in Figure 3 of Hosseinzadeh et al. (2019), which were also derived from $H\alpha$ luminosities, we find that SN 2024abvb has a higher SFR density than 10 SNe Ibn (59% of the sample) and 9 SNe IIn (57% of the sample). This places SN 2024abvb above the median SFR density of both SNe Ibn and SNe IIn environments, suggesting that the local environment is broadly consistent with, though somewhat more star-forming than, the majority of the comparison sample.

We use the far ultraviolet (FUV) emission to trace the recent (16 – 100 Myr) local star formation history. The FUV data yielded an upper limit of 20.8 mag. This value is an upper limit from our *Swift* UV observation in the *UVW2* band after using the package *uvotimsum* and following the aperture photometry procedure outlined in Section 2.0.2. The FUV magnitude was corrected for the line-of-sight MW extinction. Using Equation 3 from Karachentsev & Kaisina (2013), we obtained $\log_{10}(\text{SFR}[\text{M}_\odot \text{ yr}^{-1}]) = -1.40 \pm 0.001$, equivalent to

a SFR of $0.039 \pm 0.0001 \text{ M}_\odot \text{ yr}^{-1}$. We note that this method yields a SFR value greater than the ongoing local SFR, which is likely due to the *UVW2* band overlapping with the NUV band wavelength range leading to an overestimation of the recent local SFR. Nonetheless, this value is still smaller than the global SFR estimate of $0.10 \text{ M}_\odot \text{ yr}^{-1}$ and provides an upper bound to the recent SFR in the local environment. Compared to the SFR distribution of SNe Ibn and SESNe hosts (see Figure 10 in Warwick et al. 2025), the local SFR of SN 2024abvb lies in the bottom ~ 5 th percentile of SESNe hosts, suggesting a WR progenitor is unlikely.

As proposed by Pellegrino et al. (2022b), a progenitor less massive than a WR star and residing in a binary system would have a longer evolutionary lifetime, thereby reducing the runaway velocity required to reach the observed location of SN 2024abvb. In this scenario, binary stripping would produce a substantial amount of CSM around the progenitor, rather than the line-driven mass loss that occurs during the main-sequence stage of a massive star. Furthermore, the low host-galaxy metallicity ($\log_{10}(Z_*/Z_\odot) = -1.38^{+0.38}_{-0.34}$) implies a low progenitor metallicity, making significant line-driven mass loss unlikely for SN 2024abvb. However, this metallicity estimate is inferred from photometric measurements alone and should be treated with caution. Another possibility is extreme episodic mass loss. For example, core-collapse progenitor stars are particularly active (e.g., Zenati et al., 2025; Killestein et al., 2025), especially SNe Ibn. The progenitor stars of SN 2006jc and SN 2019uo (Foley et al., 2007; Pastorello et al., 2007; Strotjohann et al., 2021) showed luminous precursor outbursts 1 – 2 years before explosion. No precursor activity brighter than $m_r \approx 20$ mag was reported for SN 2024abvb before its discovery, suggesting that the progenitor did not experience luminous eruptive episodes before collapse. Considering the observables of SN 2024abvb, including the ejecta mass (M_{ej}) and ^{56}Ni mass (M_{Ni}) inferred from bolometric modelling, and the large projected offset of the SN from its host galaxy, we suggest the following plausible progenitor explanation: a binary system in which the primary star is of relatively low mass and undergoes significant mass loss through binary stripping before exploding within a dense, H/He-poor CSM.

5. Conclusion

We have presented the UV, optical, and NIR photometric and spectroscopic observations of SN 2024abvb, a unique Type Icn SN exhibiting C II emission in its early spectra and the largest projected offset from its host-galaxy reported to date (22.4 kpc). SN 2024abvb is so far the sixth SNe Icn discovered, providing a rare opportunity to investigate its progenitor avenues and explosion environment of this class. The key findings from our analysis are summarised here:

- SN 2024abvb reaches a peak magnitude of $M_r = -19.55 \pm 0.11$, placing it among the most luminous members of the SNe Icn class. The SN declines at a rate of $0.07 \text{ mag day}^{-1}$ in the r band, which is consistent with other known

SNe Icn (Fraser et al., 2021; Perley et al., 2022; Pellegrino et al., 2022b; Davis et al., 2023) but slow compared to SNe Ibn (Hosseinzadeh et al., 2017).

- During the first week, SN 2024abvb shows evidence of interaction with a H/He-poor, C-rich CSM in its optical spectra. Its early absence of C III $\lambda 5700$ could suggest a Type Ibn classification, but the persistent lack of He emission at late times indicates a transition from SN Ibn to SN Icn with low C ionisation, making SN 2024abvb the first known example of such an event.
- SN 2024abvb was found 22.4 kpc away from its host galaxy, which is the largest distance of the SNe Icn sample and the third largest of the SNe Ibn sources measured so far. This offset is similar to SN Ibn PS1-12sk, which also exploded in a region devoid of star formation. These atypical explosion environments suggest the possibility of a progenitor channel other than a direct collapse of WR stars, or WR-like massive stars, which are typically favoured for SNe Ibn/Icn.
- The host-galaxy of SN 2024abvb is an intermediate-mass galaxy with a stellar mass of $\log_{10}(M_*/M_\odot) = 9.66^{+0.12}_{-0.12}$ and an extremely low sSFR of $\log_{10}(\text{sSFR yr}^{-1}) = -10.62^{+0.79}_{-1.22}$. The low metallicity ($\log_{10}(Z_*/Z_\odot) = -1.38^{+0.38}_{-0.34}$), could reflect a metal-poor progenitor for SN 2024abvb, potentially limiting the role of line-driven winds in stripping its H/He envelope. This would suggest a scenario in which a low-mass star was stripped by a compact companion and exploded within a dense, H/He-poor CSM.
- We fit the combined UV, optical, and NIR light curves of SN 2024abvb with a radioactive decay + CSM interaction model, and find values of $M_{\text{ej}} \sim 2.59 M_\odot$, $M_{\text{CSM}} \sim 0.28 M_\odot$, and $M_{\text{Ni}} \sim 0.1 M_\odot$, all of which are consistent with rapidly evolving SNe Ibn (Pellegrino et al., 2022a). However, other SNe Icn show lower M_{Ni} . This diversity may arise from differences in how physical parameters are inferred or assumed for different events.
- From implanting a synthetic H α feature, we derive a local SFR density of $1.5 \times 10^{-2} M_\odot \text{ yr}^{-1} \text{ kpc}^{-2}$, consistent with typical SNe Ibn and SNe IIn hosts (Hosseinzadeh et al., 2019). *Swift* UV yield a local SFR of 0.039 ± 0.0001 , placing it in the bottom ~ 5 th percentile of SESNe host galaxies.

6. Acknowledgements

W.B.H. acknowledges support from the National Science Foundation Graduate Research Fellowship Program under Grant No. 2236415. M.D.S. is funded by the Independent Research Fund Denmark (IRFD, grant number 10.46540/2032-00022B) L.G. acknowledges financial support from CSIC, MCIN and AEI 10.13039/501100011033 under projects PID2023-151307NB-I00, PIE 20215AT016, and CEX2020-001058-M. J.T.H acknowledges support provided by NASA through the NASA Hubble Fellowship grant HST-HF2-51577.001-A awarded by the Space Telescope Science Institute, which

is operated by the Association of Universities for Research in Astronomy, Incorporated, under NASA contract NAS5-26555. D.O.J. acknowledges support from NSF grants AST-2407632, AST-2429450, and AST-2510993, NASA grant 80NSSC24M0023, and HST/JWST grants HST-GO-17128.028 and JWST-GO-05324.031, awarded by the Space Telescope Science Institute (STScI), which is operated by the Association of Universities for Research in Astronomy, Inc., for NASA, under contract NAS5-26555.

Based in part on data acquired at the ANU 2.3-metre telescope, under proposal ID: 2425062, 2425126, 2425128. The automation of the telescope was made possible through an initial grant provided by the Centre of Gravitational Astrophysics and the Research School of Astronomy and Astrophysics at the Australian National University and through a grant provided by the Australian Research Council through LE230100063. The Lens proposal system is maintained by the AAO Research Data & Software team as part of the Data Central Science Platform. We acknowledge the traditional custodians of the land on which the telescope stands, the Gamilaraay people, and pay our respects to elders past and present.

The authors wish to recognise and acknowledge the significant cultural role and reverence that the summit of Maunakea has always had within the indigenous Hawaiian community. We are most fortunate to have the opportunity to conduct observations from this mountain.

Some of the data presented herein were obtained at the Keck Observatory, which is a private 501(c) (3) nonprofit organization operated as a scientific partnership among the California Institute of Technology, the University of California, and the National Aeronautics and Space Administration. The Observatory was made possible by the generous financial support of the W. M. Keck Foundation.

UKIRT is owned by the University of Hawaii (UH) and operated by the UH Institute for Astronomy.

The Infrared Telescope Facility, which is operated by the University of Hawaii under contract 80HQTR24DA010 with the National Aeronautics and Space Administration.

Parts of this research were supported by the Australian Research Council Centre of Excellence for Gravitational Wave Discovery (OzGrav), through project number CE230100016.

B.E.T. acknowledges support from the Kavli Foundation.

IMACS data were obtained while A.P. was supported by a Carnegie Fellowship through the Observatories of the Carnegie Institute for Science.

References

Afsariardchi, N., Drout, M. R., Khatami, D. K., et al. 2021, *ApJ*, 918, 89
 Anderson, J. P. 2019, *A&A*, 628, A7
 Angus, C. R., Smith, M., Sullivan, M., et al. 2019, *MNRAS*, 487, 2215
 Arnett, W. D. 1982, *ApJ*, 253, 785
 Asplund, M., Grevesse, N., Sauval, A. J., & Scott, P. 2009, *ARA&A*, 47, 481
 Barbary, K. 2021, nestle: Nested sampling algorithms for evaluating Bayesian evidence, *Astrophysics Source Code Library*, record ascl:2103.022
 Bellm, E. C., Kulkarni, S. R., Graham, M. J., et al. 2019, *PASP*, 131, 018002
 Botyánszki, J., Kasen, D., & Plewa, T. 2018, *ApJ*, 852, L6

Breeveld, A. A., Landsman, W., Holland, S. T., et al. 2011, in American Institute of Physics Conference Series, Vol. 1358, Gamma Ray Bursts 2010, ed. J. E. McEnery, J. L. Racusin, & N. Gehrels (AIP), 373–376

Breeveld, A. A., Curran, P. A., Hoversten, E. A., et al. 2010, MNRAS, 406, 1687

Brown, W. R. 2015, ARA&A, 53, 15

Burns, C., Hsiao, E., Suntzeff, N., et al. 2021, The Astronomer's Telegram, 14441, 1

Burrows, D. N., Hill, J. E., Nousek, J. A., et al. 2005, Space Sci. Rev., 120, 165

Carr, A., Davis, T. M., Camilleri, R., et al. 2024, PASA, 41, e068

Casali, M., Adamson, A., Alves de Oliveira, C., et al. 2007, A&A, 467, 777

Chambers, K. C., Magnier, E. A., Metcalfe, N., et al. 2016, arXiv e-prints, arXiv:1612.05560

Chatzopoulos, E., Wheeler, J. C., & Vinko, J. 2012, ApJ, 746, 121

Chatzopoulos, E., Wheeler, J. C., Vinko, J., Horvath, Z. L., & Nagy, A. 2013, ApJ, 773, 76

Childress, M. J., Vogt, F. P. A., Nielsen, J., & Sharp, R. G. 2014, Ap&SS, 349, 617

Coulter, D. A., Foley, R. J., Kilpatrick, C. D., et al. 2017, Science, 358, 1556

Cushing, M. C., Vacca, W. D., & Rayner, J. T. 2004, PASP, 116, 362

Dastidar, R., Pignata, G., Dukiya, N., et al. 2025, A&A, 703, A224

Davis, K. W., Taggart, K., Tinyanont, S., et al. 2023, MNRAS, 523, 2530

Dessart, L., Hillier, D. J., & Kuncarayakti, H. 2022, A&A, 658, A130

Dessart, L., Livne, E., & Waldman, R. 2010, MNRAS, 405, 2113

Dey, A., Schlegel, D. J., Lang, D., et al. 2019, AJ, 157, 168

Dong, Y., Villar, V. A., Nugent, A., et al. 2025, arXiv e-prints, arXiv:2511.03926

Dopita, M., Hart, J., McGregor, P., et al. 2007, Ap&SS, 310, 255

Dopita, M., Rhee, J., Farage, C., et al. 2010, Ap&SS, 327, 245

Dressler, A., Bigelow, B., Hare, T., et al. 2011, PASP, 123, 288

Drout, M. R., Götzberg, Y., Ludwig, B. A., et al. 2023, Science, 382, 1287

Eldridge, J. J., Fraser, M., Smartt, S. J., Maund, J. R., & Crockett, R. M. 2013, MNRAS, 436, 774

Eldridge, J. J., Langer, N., & Tout, C. A. 2011, MNRAS, 414, 3501

Ercolino, A., Jin, H., Langer, N., & Dessart, L. 2025, A&A, 696, A103

Farias, D., Gall, C., Villar, V. A., et al. 2025, arXiv e-prints, arXiv:2511.12362

Fausnaugh, M. M., Valley, P. J., Tucker, M. A., et al. 2023, ApJ, 956, 108

Filippenko, A. V. 1997, ARA&A, 35, 309

Flewelling, H. A., Magnier, E. A., Chambers, K. C., et al. 2020, ApJS, 251, 7

Foley, R. J., Smith, N., Ganeshalingam, M., et al. 2007, ApJ, 657, L105

Foreman-Mackey, D. 2015, George: Gaussian Process regression, Astrophysics Source Code Library, record ascl:1511.015

Foreman-Mackey, D., Hogg, D. W., Lang, D., & Goodman, J. 2013, PASP, 125, 306

Fraser, M. 2020, Royal Society Open Science, 7, 200467

Fraser, M., Stritzinger, M. D., Brennan, S. J., et al. 2021, arXiv e-prints, arXiv:2108.07278

Fukugita, M., Ichikawa, T., Gunn, J. E., et al. 1996, AJ, 111, 1748

Fulton, M., Bulger, J., Huber, M. E., et al. 2022, Transient Name Server AstroNote, 198, 1

Gal-Yam, A. 2017, in Handbook of Supernovae, ed. A. W. Alsabti & P. Murdin, 195

Gal-Yam, A., Yaron, O., & Schulze, S. 2024a, Transient Name Server AstroNote, 239, 1

Gal-Yam, A., Bruch, R., Schulze, S., et al. 2022, Nature, 601, 201

Gal-Yam, A., Schulze, S., Yang, Y., et al. 2024b, Transient Name Server AstroNote, 240, 1

Gangopadhyay, A., Dukiya, N., Moriya, T. J., et al. 2025a, MNRAS, 537, 2898

Gangopadhyay, A., Sollerman, J., Tsalapatas, K., et al. 2025b, MNRAS, arXiv:2506.10700

Gehrels, N., Chincarini, G., Giommi, P., et al. 2004, ApJ, 611, 1005

Gogarten, S. M., Dalcanton, J. J., Murphy, J. W., et al. 2009, ApJ, 703, 300

Götberg, Y., de Mink, S. E., & Groh, J. H. 2017, A&A, 608, A11

Groot, P. J., Bloemen, S., Vreeswijk, P. M., et al. 2024, PASP, 136, 115003

Heger, A., Fryer, C. L., Woosley, S. E., Langer, N., & Hartmann, D. H. 2003, ApJ, 591, 288

Hinkle, J. 2023, Transient Name Server Classification Report, 2023-2507, 1

Hinton, S. R., Davis, T. M., Lidman, C., Glazebrook, K., & Lewis, G. F. 2016, Astronomy and Computing, 15, 61

Hodgkin, S. T., Irwin, M. J., Hewett, P. C., & Warren, S. J. 2009, MNRAS, 394, 675

Hoogendam, W. B., Hinkle, J. T., Shappee, B. J., et al. 2024, MNRAS, 530, 4501

Hoogendam, W. B., Ashall, C., Jones, D. O., et al. 2025a, ApJ, 988, 209

Hoogendam, W. B., Jones, D. O., Ashall, C., et al. 2025b, The Open Journal of Astrophysics, 8, 120

Hosseinzadeh, G., McCully, C., Zabludoff, A. I., et al. 2019, ApJ, 871, L9

Hosseinzadeh, G., Arcavi, I., Valenti, S., et al. 2017, ApJ, 836, 158

Hsiao, E. Y., Phillips, M. M., Marion, G. H., et al. 2019, PASP, 131, 014002

Hu, M., Yan, S., Wang, X., et al. 2026, arXiv e-prints, arXiv:2601.01333

Huber, M., Chambers, K. C., Flewelling, H., et al. 2015, The Astronomer's Telegram, 7153, 1

Johnson, B. D., Leja, J., Conroy, C., & Speagle, J. S. 2021, ApJS, 254, 22

Jones, D. O., McGill, P., Manning, T. A., et al. 2024, arXiv e-prints, arXiv:2410.17322

Kaiser, N., Burgett, W., Chambers, K., et al. 2010, in Society of Photo-Optical Instrumentation Engineers (SPIE) Conference Series, Vol. 7733, Ground-based and Airborne Telescopes III, ed. L. M. Stepp, R. Gilmozzi, & H. J. Hall, 77330E

Karachentsev, I. D., & Kaisina, E. I. 2013, AJ, 146, 46

Kennicutt, Jr., R. C. 1998, ARA&A, 36, 189

Killestein, T. L., Pursiainen, M., Kotak, R., et al. 2025, arXiv e-prints, arXiv:2510.27631

Ko, T., Kinugawa, T., Tsuna, D., Hirai, R., & Takei, Y. 2025a, arXiv e-prints, arXiv:2506.00931

—. 2025b, MNRAS, arXiv:2506.00931

Kreuzer, S., Irrgang, A., & Heber, U. 2020, A&A, 637, A53

Krisciunas, K., Contreras, C., Burns, C. R., et al. 2017, AJ, 154, 211

Kuncarayakti, H., Maeda, K., Dessart, L., et al. 2022, ApJ, 941, L32

Lantz, B., Aldering, G., Antilogus, P., et al. 2004, in Society of Photo-Optical Instrumentation Engineers (SPIE) Conference Series, Vol. 5249, Optical Design and Engineering, ed. L. Mazuray, P. J. Rogers, & R. Wartmann, 146–155

Leja, J., Johnson, B. D., Conroy, C., et al. 2019, ApJ, 877, 140

Lyman, J. D., Bersier, D., James, P. A., et al. 2016, MNRAS, 457, 328

Ma, X., Wang, X., Mo, J., et al. 2025, A&A, 698, A305

Madau, P., & Dickinson, M. 2014, ARA&A, 52, 415

Maeda, K., & Moriya, T. J. 2022, ApJ, 927, 25

Martin, D. C., Fanson, J., Schiminovich, D., et al. 2005, ApJ, 619, L1

Masci, F. J., Laher, R. R., Rusholme, B., et al. 2019, PASP, 131, 018003

—. 2023, arXiv e-prints, arXiv:2305.16279

Maund, J. R., Pastorello, A., Mattila, S., Itagaki, K., & Boles, T. 2016, ApJ, 833, 128

Medler, K., Ashall, C., Shahbandeh, M., et al. 2025, arXiv e-prints, arXiv:2505.18507

Metzger, B. D. 2022, ApJ, 932, 84

Modjaz, M., Gutiérrez, C. P., & Arcavi, I. 2019, Nature Astronomy, 3, 717

Moriya, T. J. 2014, A&A, 564, A83

Morrissey, P., Matuszewski, M., Martin, D. C., et al. 2018, ApJ, 864, 93

Nagao, T., Kuncarayakti, H., Maeda, K., et al. 2023, A&A, 673, A27

Panjikov, S., Auchettl, K., Shappee, B. J., et al. 2024, PASA, 41, e059

Pastorello, A., Smartt, S. J., Mattila, S., et al. 2007, Nature, 447, 829

Pastorello, A., Mattila, S., Zampieri, L., et al. 2008, MNRAS, 389, 113

Pastorello, A., Benetti, S., Brown, P. J., et al. 2015a, MNRAS, 449, 1921

Pastorello, A., Hadjiyska, E., Rabinowitz, D., et al. 2015b, MNRAS, 449, 1954

Pellegrino, C., Howell, D. A., Vinkó, J., et al. 2022a, *ApJ*, 926, 125

Pellegrino, C., Howell, D. A., Terreran, G., et al. 2022b, *The Astrophysical Journal*, 938, 73, arXiv:2205.07894 [astro-ph]

Pellegrino, C., Modjaz, M., Takei, Y., et al. 2024, *ApJ*, 977, 2

Perley, D. A., Fremling, C., Sollerman, J., et al. 2020, *ApJ*, 904, 35

Perley, D. A., Sollerman, J., Schulze, S., et al. 2022, *ApJ*, 927, 180

Pessi, T., Desai, D. D., Prieto, J. L., et al. 2025, *A&A*, 703, A34

Peterson, E. R., Jones, D. O., Scolnic, D., et al. 2023, *MNRAS*, 522, 2478

Podsiadlowski, P., Joss, P. C., & Hsu, J. J. L. 1992, *ApJ*, 391, 246

Poole, T. S., Breeveld, A. A., Page, M. J., et al. 2008, *MNRAS*, 383, 627

Price, I., Nielsen, J., Lidman, C., et al. 2024, *PASA*, 41, e057

Pursiainen, M., Leloudas, G., Schulze, S., et al. 2023, *ApJ*, 959, L10

Rabinak, I., & Waxman, E. 2011, *ApJ*, 728, 63

Rayner, J. T., Toomey, D. W., Onaka, P. M., et al. 2003, *PASP*, 115, 362

Renzo, M., Zapartas, E., de Mink, S. E., et al. 2019, *A&A*, 624, A66

Rest, A., Stubbs, C., Becker, A. C., et al. 2005, *ApJ*, 634, 1103

Rest, S., Rest, A., Kilpatrick, C. D., et al. 2025, *ApJ*, 979, 114

Roming, P. W. A., Kennedy, T. E., Mason, K. O., et al. 2005, *Space Sci. Rev.*, 120, 95

Sand, D. J., Graham, M. L., Botyánszki, J., et al. 2018, *ApJ*, 863, 24

Sand, D. J., Sarbadhicary, S. K., Pellegrino, C., et al. 2021, *ApJ*, 922, 21

Sanders, N. E., Soderberg, A. M., Foley, R. J., et al. 2013, *ApJ*, 769, 39

Sarin, N., Hübner, M., Omand, C. M. B., et al. 2024, *MNRAS*, 531, 1203

Schechter, P. L., Mateo, M., & Saha, A. 1993, *PASP*, 105, 1342

Schlafly, E. F., & Finkbeiner, D. P. 2011, *ApJ*, 737, 103

Schlegel, E. M. 1990, *MNRAS*, 244, 269

Schulze, S., Yaron, O., Sollerman, J., et al. 2022, *VizieR Online Data Catalog: The PTF core-collapse SN host-galaxy sample. I.* (Schulze+, 2021), *VizieR On-line Data Catalog: J/ApJS/255/29*. Originally published in: 2021ApJS..255...29S, doi:10.26093/cds/vizier.22550029

Schulze, S., Gal-Yam, A., Dessart, L., et al. 2024, arXiv e-prints, arXiv:2409.02054

Shahbandeh, M., Hsiao, E. Y., Ashall, C., et al. 2022, *ApJ*, 925, 175

Shivvers, I., Zheng, W., Van Dyk, S. D., et al. 2017, *MNRAS*, 471, 4381

Simcoe, R. A., Burgasser, A. J., Bernstein, R. A., et al. 2008, in *Society of Photo-Optical Instrumentation Engineers (SPIE) Conference Series*, Vol. 7014, *Ground-based and Airborne Instrumentation for Astronomy II*, ed. I. S. McLean & M. M. Casali, 70140U

Skrutskie, M. F., Cutri, R. M., Stiening, R., et al. 2006, *AJ*, 131, 1163

Smith, K. W., Smartt, S. J., Young, D. R., et al. 2020, *PASP*, 132, 085002

Smith, N. 2014, *ARA&A*, 52, 487

—. 2017, in *Handbook of Supernovae*, ed. A. W. Alsabti & P. Murdin, 403

Stritzinger, M., Fraser, M., Pastorello, A., et al. 2024, *Transient Name Server Classification Report*, 2024-4674, 1

Strotjohann, N. L., Ofek, E. O., Gal-Yam, A., et al. 2021, *ApJ*, 907, 99

Sun, N.-C., Maund, J. R., Hirai, R., Crowther, P. A., & Podsiadlowski, P. 2020, *MNRAS*, 491, 6000

The INTEL Collaboration, Anderson, J. P., Aster, C., et al. 2026, arXiv e-prints, arXiv:2602.00389

Thornton, I., Villar, V. A., Gomez, S., & Hosseinzadeh, G. 2024, *Research Notes of the American Astronomical Society*, 8, 48

Tominaga, N., Limongi, M., Suzuki, T., et al. 2008, *ApJ*, 687, 1208

Tonry, J., Denneau, L., Weiland, H., et al. 2023, *Transient Name Server Discovery Report*, 2023-2485, 1

—. 2024, *Transient Name Server Discovery Report*, 2024-4579, 1

Tonry, J. L., Denneau, L., Heinze, A. N., et al. 2018, *PASP*, 130, 064505

Tremonti, C. A., Heckman, T. M., Kauffmann, G., et al. 2004, *ApJ*, 613, 898

Tucker, M. A., Shappee, B. J., Vallet, P. J., et al. 2020, *MNRAS*, 493, 1044

Tucker, M. A., Shappee, B. J., Huber, M. E., et al. 2022, *PASP*, 134, 124502

Vallely, P. J., Kochanek, C. S., Stanek, K. Z., Fausnaugh, M., & Shappee, B. J. 2021, *MNRAS*, 500, 5639

Villar, V. A., Berger, E., Metzger, B. D., & Guillochon, J. 2017, *ApJ*, 849, 70

Wang, B., Leja, J., Bezanson, R., et al. 2023, *ApJ*, 944, L58

Warwick, B., Lyman, J., Pursiainen, M., et al. 2025, *MNRAS*, 536, 3588

Woosley, S. E. 2017, *ApJ*, 836, 244

Wright, E. L., Eisenhardt, P. R. M., Mainzer, A. K., et al. 2010, *AJ*, 140, 1868

Wu, S. C., & Fuller, J. 2022, *ApJ*, 940, L27

Yamanaka, M., & Nagayama, T. 2025, *ApJ*, 990, L44

Yaron, O., & Gal-Yam, A. 2012, *PASP*, 124, 668

Yoon, S.-C. 2017, *MNRAS*, 470, 3970

Yoon, S. C., Woosley, S. E., & Langer, N. 2010, *ApJ*, 725, 940

York, D. G., Adelman, J., Anderson, Jr., J. E., et al. 2000, *AJ*, 120, 1579

Zapartas, E., de Mink, S. E., Izzard, R. G., et al. 2017, *A&A*, 601, A29

Zenati, Y., Wang, Q., Bobrick, A., et al. 2025, *ApJ*, 992, 9

Appendix 1. Host Galaxy

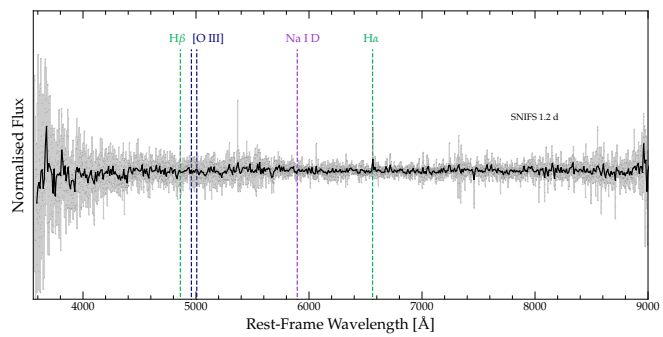


Figure A1. Host galaxy spectrum of SN 2024abvb taken 1.2 days after maximum σ -band brightness. We find weak $\text{H}\alpha$, $\text{H}\beta$, and $[\text{O III}]$ emission lines. The lack of Na I D absorption indicates that there is minor or no host-galaxy extinction present.

Appendix 2. Log of spectroscopic observations

In Table A1, we present the optical and NIR spectroscopic observations of SN 2024abvb.

Appendix 3. Radioactive Decay Model

The radioactive decay model assumes that the light curve is powered by the decay chain ^{56}Ni to ^{56}Co to ^{56}Fe . We fit the analytical model of Arnett (1982) to the UVOIR multi-band light curve, assuming homologous expansion with a uniform density profile for the ejecta. The optical (electron scattering) opacity was fixed to $\kappa_o = 0.04 \text{ cm}^2 \text{ g}^{-1}$ following Pellegrino et al. (2022b), and the gamma opacity was fixed to $\kappa_\gamma = 0.08 \text{ cm}^2 \text{ g}^{-1}$ (Rabinak & Waxman, 2011). We impose the physical constraint that f_{Ni} does not exceed the total ejecta mass. The free parameters in the fit include the nickel fraction f_{Ni} , the ejecta mass M_{ej} , ejecta velocity V_{ej} , and the temperature floor T_{floor} .

The best-fit light curve and corresponding corner plot are shown in Figure A2 and the derived parameters are presented in Table A2. Overall, the radioactive decay model is

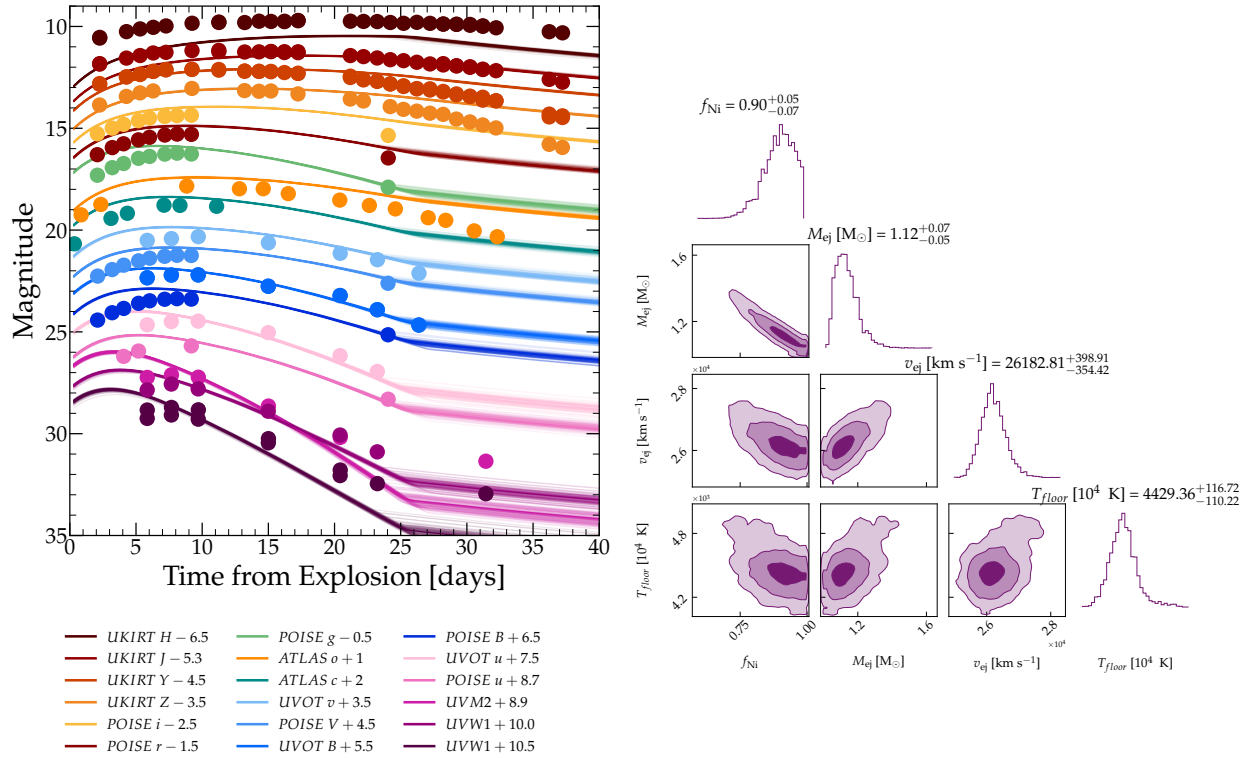


Figure A2. *Left:* The best-fit multi-band light curves of SN 2024abvb using the Arnett model (Arnett, 1982). *Right:* The corner plot of the Arnett model fit to the multi-band light curve of SN 2024abvb in Redback.

Table A1. Log of spectroscopic observations for SN 2024abvb.

UT Date	MJD	Telescope	Instrument	Range [Å]
<i>Optical</i>				
2024-11-23	60637.4	UH 2.2m	SNIFS	3280-8750
2024-11-26	60640.4	UH 2.2m	SNIFS	3280-8750
2024-11-27	60641.9	NOT	ALFOSC	3460-9300
2024-12-02	60646.4	ANU 2.3m	WiFeS	3920-8680
2024-12-02	60646.9	NOT	ALFOSC	3530-9330
2024-12-05	60649.4	ANU 2.3m	WiFeS	3920-8590
2024-12-08	60652.4	ANU 2.3m	WiFeS	3920-8590
2024-12-10	60654.1	Magellan-Baade	IMACS	4090-9010
2024-12-16	60660.5	ANU 2.3m	WiFeS	3920-8590
2024-12-19	60663.2	UH 2.2m	SNIFS	3280-8750
2024-12-22	60666.3	UH 2.2m	SNIFS	3280-8750
2024-12-23	60667.2	Keck II	KCWI	3160-8560
<i>NIR</i>				
2024-12-08	60652.0	Magellan-Baade	FIRE	7500-23300
2024-12-18	60662.3	SpeX	IRTF	6800-24300

a reasonable fit to the multiband light curves; however, it overestimates the rise to peak (0 – 10 days from explosion), particularly in the optical and UV bands, and slightly overfits the decline rate. A ^{56}Ni mass of M_{Ni} of $\simeq 1.01 M_{\odot}$ ($> 90\%$) is required to reproduce a reasonable fit to the light curve, which is unusually high for CCSNe. By comparison, Anderson (2019) report a median $M_{\text{Ni}} < 0.4 M_{\odot}$ across all CCSNe types, the derived value also exceeds the high-end distribution of SESNe (Lyman et al., 2016). Relative to other SNe Icn, SN 2024abvb is an order of magnitude greater (see Figure 8 in Pellegrino et al. (2022b)). A lower limit on the ^{56}Ni mass can be estimated from the late-time bolometric luminosity using the relation of Arnett (1982), as applied by Davis et al. (2023). Assuming instantaneous γ -ray trapping and that SN 2024abvb is powered by ^{56}Ni at late times, the measured bolometric luminosity ($\sim 2 \times 10^{41} \text{ erg s}^{-1}$) implies a ^{56}Ni mass of $\approx 0.007 M_{\odot}$, which is smaller than typical values for SESNe (Lyman et al., 2016; Afsariardchi et al., 2021). From the bolometric light curve, we also estimate an ejecta velocity (v_{ej}) of $\sim 26000 \text{ km s}^{-1}$, higher but comparable in order of magnitude to the photospheric velocity ($\sim 18000 \text{ km s}^{-1}$). This is similar to SN 2021csp, for which Pellegrino et al. (2022b) derived $v_{\text{ej}} \sim 23000 \text{ km s}^{-1}$. However, the lack of spectral features exceeding $> 2000 \text{ km s}^{-1}$ presents a clear discrepancy. As such, these results indicate that radioactive decay alone is unlikely to be the dominant power source of SN 2024abvb.

Table A2. Best-fit parameters for the Arnett model as described in Section [Appendix 3](#).

Parameters	Priors	Best-Fitted Values
f_{Ni}	$\mathcal{U}[0.01, 0.99]$	$0.90^{+0.05}_{-0.07}$
$M_{ej} [M_{\odot}]$	$\log \mathcal{U}[0.01, 2]$	$1.12^{+0.07}_{-0.05}$
$V_{ej} [\text{km s}^{-1}]$	$\mathcal{U}[10^2, 5 \times 10^4]$	$26182.81^{+398.91}_{-354.42}$
$T_{\text{floor}} [\text{K}]$	$\mathcal{U}[10^3, 10^4]$	$4429.36^{+116.72}_{-110.22}$